Available online at www.sciencedirect.com
ScienceDirect
Trans. Nonferrous Met. Soc. China 35(2025) 765−787
Transactions of Nonferrous Metals Society of China
www.tnmsc.cn

Effects of Zr addition on mechanical properties and in vitro degradation behavior of Mg−1.0Yb cast alloy

Zhuo-zhang WEN, Lu LI, Xue BAI, Wei ZHOU, Zhen-ni ZHOU, Peng XUE, Jing LI, Xian-quan JIANG

School of Materials and Energy, Southwest University, Chongqing 400715, China

Received 15 June 2023; accepted 19 October 2023

Abstract: The effects of Zr addition on the mechanical properties and in vitro degradation behavior of Mg−1.0Yb−*x*Zr (*x*=0, 0.2, 1.0, and 1.53, wt.%) cast alloys were investigated. The results indicated that with increasing Zr addition, a much refined and homogeneous equiaxed grain structure was achieved from a typical columnar grain structure, in companion with the appearance and coarsening of Zr-rich particles. Subsequent electrochemical and immersion tests demonstrated that the corrosion of the alloy was Zr-addition dependent. A trace or excessive Zr addition caused severe localized corrosion attacks, whereas Zr-free and 1.0 Zr alloyed counterparts were generally corroded uniformly. The good combination of mechanical properties and corrosion resistance of the Mg−1.0Yb−1.0Zr alloy was resulted from the refined and homogeneous equiaxed grain structure and fine dispersed Zr-rich particles, thus improving the comprehensive mechanical properties by grain refinement and reducing corrosion rate by generating a more stable and compact passivation layer during long-term immersion.

Key words: Mg−Yb alloy; zirconium addition; microstructure; mechanical properties; corrosion behavior

1 Introduction

Magnesium (Mg) is recognized as the most promising biomedical material due to its excellent performance both in the biocompatibility and biodegradation ability [1]. However, the rapid degradation in a physiological environment often results in a loss of mechanical integrity prior to the complete healing of damaged tissues, severely limiting its wide application as biodegradable implants [2,3]. Therefore, it is of great significance to improve the biocorrosion resistance of Mg alloys for biomedical applications.

As well acknowledged, zirconium (Zr) is a potent grain refiner for Mg alloys. Both Zr and Mg are HCP crystal structures with close lattice constants (Mg: a=0.321 nm, c=0.521 nm; Zr: a= 0.323 nm, c=0.514 nm), which renders Zr acting as ideal heterogeneous nucleation sites for the Mg matrix. When the Zr addition is up to the solubility limit in Mg (0.58 wt.% at the peritectic temperature of 654 °C), the peritectic reaction will occur with the Mg matrix solidifying around Zr-rich cores, greatly refining the microstructure with equiaxed magnesium grains. Recently, a large body of studies demonstrated that a proper Zr addition in Mg alloy can effectively modify the microstructure, finally achieving the enhancement in corrosion resistance and mechanical properties. SUN et al [4] found that the size and distribution of the Zr-rich particles significantly affected the corrosion behavior and a good combination of mechanical strength and corrosion resistance was achieved with 0.42% Zr addition. JAFARI and AMIRYAVARI [5] observed that Zr addition significantly refined the grain structure of as-cast AZ63 alloy, thus improving the corrosion resistance. However, when the Zr addition

Corresponding author: Lu LI, Tel: +86-23-68253204, E-mail: liluswu@gmail.com
DOI: https://doi.org/10.1016/S1003-6326(24)66713-0
1003-6326/© 2025 The Nonferrous Metals Society of China. Published by Elsevier Ltd & Science Press
This is an open access article under the CC BY-NC-ND license (http://creativecommons.org/licenses/by-nc-nd/4.0/)

exceeded 0.5 wt.%, the corrosion property deteriorated due to the formation of Al_2Zr compounds. KIANI et al [6] believed that the low corrosion rate of the extruded Mg−0.5Zr−3Sr alloy was mainly attributed to the accumulation of dense $Mg_{17}Sr_2$ particles at grain boundaries, which prevented the early deposition of the $Mg(OH)_2$ protective layer. Although the effect of Zr addition on Mg alloys has been studied extensively [7,8], the effect of Zr concentration on the microstructure, biodegradability, and mechanical properties of Mg−Yb binary alloys has not been identified.

Recent studies have demonstrated that the addition of rare earth elements can effectively improve the strength of Mg alloys without reducing the corrosion resistance [9,10]. Among these attempts, the heavy rare earth element ytterbium (Yb) has attracted increasing interest and a series of Yb-containing Mg alloys with good comprehensive performance have been developed [11−13]. In our previous investigation [14], Mg−5.8Zn−0.5Zr−*x*Yb (*x*=0, 1.0, and 2.0 wt.%) alloys were prepared, and the peak-aged Mg−5.8Zn−0.5Zr−2.0Yb sample exhibited favorable mechanical properties due to much finer and denser precipitates developed, which simultaneously improved the biodegradation resistance by generating a more compact and uniform protective film. Further biocompatibility testing suggested that all the aged samples possessed good hemocompatibility [15]. To further clarify the effect of the sole addition of Yb on the Mg matrix, the Mg−Yb binary alloys with different Yb contents of 0.5, 1.0, and 2.0 wt.% were developed, focusing on Yb addition on microstructure development and tensile properties [16]. The results indicated that the grain refinement was pronounced with increasing Yb addition, but the as-cast grain morphology retained the typical columnar type, just like the Yb-free pure Mg matrix. Although a high addition of 2.0 wt.% Yb significantly improved the tensile strength, the ductility deteriorated due to the coarseness of Yb-containing phases. However, the Mg−1.0Yb alloy presented a more homogeneous grain structure exhibiting a favorable balance between strength and ductility. In this sense, the Mg−1.0Yb alloy may have great potential for further enhancements in mechanical strength and corrosion resistance given a coarse and columnar-type grain structure still retained. Accordingly, a novel Mg−Yb−Zr alloy was prepared and it was expected that the grain structure along with phase size and distribution would be changed by Zr addition.

In this work, four as-cast Mg−1.0Yb−*x*Zr (*x*= 0, 0.2, 1.0, and 1.5 wt.%) alloys were prepared and investigated to better understand the effects of different levels of Zr addition on the microstructure evolution, mechanical properties, biodegradation resistance, and cytotoxicity of this low-RE-alloyed Mg−1.0Yb alloys. The present work may shed light on developing high-mechanical, biocorrosion-resistant, and biocompatible low RE-containing Mg−Yb-based alloys via a cost-effective Zr addition.

2 Experimental

2.1 Materials preparation and characterization

Mg−Yb−Zr alloys with nominal composition of Mg−1.0Yb−*x*Zr (*x*=0, 0.2, 1.0, and 1.5 wt.%, hereafter denoted as 0 Zr, 0.2 Zr, 1.0 Zr, and 1.5 Zr alloys, respectively) were melted in a crucible furnace using pure Mg, Mg−30%Zr, Mg−15%Yb, and protected by a mixed atmosphere of SF_6 (10 vol.%) and CO_2 (Bal.). The as-cast ingots were machined with a geometric size of 10 mm × 10 mm × 3 mm and successively grounded with a series of SiC abrasive paper (from 400 to 2000 grid), and then etched with an etchant of 5 g picric acid, 6 mL acetic acid, 80 mL alcohol, and 10 mL water. The samples were observed by ICX4IM optical microscopy (OM) and scanning electron microscopy (SEM, JSM−6610). The electron backscatter diffraction (EBSD, Oxford Instruments AZtecHKL) was used to characterize the microstructures. Using the EBSD data, in-grain misorientation axes (IGMA) were calculated. After immersion tests, the collected corrosion products were dried at 80 °C for 3 h, and then the samples were ground into powder. The phase constituents of the corrosion products were analyzed by X-ray diffraction (XRD, Rigaku D/Max 2500), and X-ray photoelectron spectroscopy measurement (XPS, Axis Supra) was used to evaluate the surface chemical composition. The spectra calibration, processing, and fitting routines were done using Advantage software.

2.2 Electrochemical test

The electrochemical tests were carried out on an electrochemical workstation (CHI660E) and the simulated body fluid (SBF solution) with a constant temperature of (37±0.5) °C and an initial pH value of ~7.3 was prepared for the examinations. The SBF solution with ion concentrations nearly equal to those of human blood plasma was used. The chemical compositions are listed in Table 1 [17]. The samples for the electrochemical test were sealed by using epoxy with an exposed area of ~1 cm^2 and a standard three-electrode cell was used. A classical three-electrode cell was used with a platinum plate as the counter electrode, a saturated calomel electrode (SCE) as the reference electrode and the testing samples acted as the working electrodes. The polarization curves were acquired at a scanning rate of 1 mV/s and the electrochemical impedance spectrum (EIS) was evaluated at a disturbing potential of 10 mV over a frequency range of 10^{-2}−10^5 Hz. The ZsimpWin software was used for the fitting and analysis of the EIS spectra. The electrochemical parameters such as the corrosion potential (φ_{corr}(vs SCE), V) and corrosion current density (J_{corr}, μA/cm^2) were estimated by Tafel extrapolation. The polarization resistance, R_p, was used to derive a first estimate of the J_{corr}, using the following equation [18]:

$$R_p=\frac{\beta_a\beta_c}{2.3(\beta_a+\beta_c)J_{corr}} \tag{1}$$

where β_a and β_c are the anodic and cathodic Tafel slopes, respectively. The corresponding corrosion rate, η_{corr} (mm/a), was evaluated by using the following equation [19,20]:

$$\eta_{corr}=22.85J_{corr} \tag{2}$$

2.3 Immersion test

All the cylinder samples (d10 mm × 10 mm) were grounded with SiC paper up to 3000 grit, cleaned ultrasonically in ethanol and distilled water, and then dried in the air. The immersion tests were conducted in the SBF solution at (37±0.5) °C for 24 and 240 h. Then, the 1.0Zr sample was further immersed for 24, 168, 240, 480 and 720 h to track the corrosion evolution. The ratio of media volume to the sample surface was 20 mL/cm^2. After immersion, all samples were cleaned with distilled water and dried in warm flowing air. The samples were ultrasonically cleaned in a solution of 200 g/L Cr_2O_3 and 10 g/L $AgNO_3$ for 10 min to remove corrosion products. The average corrosion rate was calculated using Eq. (3) [21]:

$$v=\frac{Kw}{At\rho} \tag{3}$$

where v is the average corrosion rate (mm/a), K is a constant of coefficient (K=8.76×10^4), w is the mass loss of corrosion during immersion (g), A is the surface area exposed to the solution (cm^2), t is the exposure time (h), and ρ is the density of the material (g/cm^3).

Table 1 Ion concentration of SBF solution in present study and its comparison with that of blood plasma [17]

Ion	Ion concentration/(mmol·L^{-1})	
	Blood plasma	SBF
Na^+	142.0	142.0
K^+	5.0	5.0
Mg^{2+}	1.5	1.5
Ca^{2+}	2.5	2.5
Cl^-	103.0	147.8
HCO_3^-	27.0	4.2
HPO_4^{2-}	1.0	1.0
SO_4^{2-}	0.5	0.5
pH	7.2−7.4	7.3

2.4 In vitro cytocompatibility test

In vitro cytotoxicity test was conducted by using human umbilical vein endothelial cells (HUVECs) through 3-[4,5-dimethylthiazol-2-yl]-2,5 diphenyl tetrazolium bromide (MTT) assay. Firstly, the alloy was incubated with the cell culture medium at a specific volume for 72 h. Subsequently, the medium was extracted and further diluted ten-fold. Then, HUVECs in a 96-well plate were incubated with the diluent (200 mL per well) for 24 and 72 h, respectively, and the cell survival rate was thereby measured. For the hemolysis test, erythrocytes were purified from mouse whole blood through centrifugation. After incubation with the diluted extract, the optical absorption of supernatants at 570 nm was measured to calculate the hemolysis rate.

2.5 Mechanical properties measurements

Mechanical properties were evaluated by tensile tests. Tensile samples were machined with a

gauge length of 30 mm and a cross-section diameter of 6 mm according to ASTM B557 M−02a. The tensile tests were conducted at an initial strain rate of 10^{-3} s^{-1} and ambient temperature by using a CMT5504 tensile test machine, and the fracture morphology was examined by SEM (JSM−6610). In each condition, three specimens for tensile tests were prepared and evaluated.

3 Results

3.1 Microstructure

Figure 1 displays the optical micrographs of as-cast Mg−1.0Yb alloys with different Zr contents of 0, 0.2, 1.0, and 1.5 wt.%. It was evident that Zr played a significant role in changing grain morphology and refining gain size. With increasing Zr addition, the typical columnar structure gradually evolved into equiaxed grains along with an obvious decrease in grain size from ~219 μm in the Zr-free sample to ~62 and ~54 μm in the cases of Mg−1.0Yb−1.0Zr and Mg−1.0Yb−1.5Zr alloys, respectively. This phenomenon revealed that Zr was a potent nucleation agent in this novel Mg−1.0Yb alloy and just a low content of 1.0 wt.% addition can achieve a complete and fine equiaxed grain structure. Moreover, Figs. 1(a) and (b), as representatives of Zr-free and a trace amount of Zr-added samples, show negligible secondary phases both in grain interiors and at grain boundaries, while in the cases of a slightly excessive addition (Fig. 1(c)) and heavy-alloyed (Fig. 1(d)) samples, the isolated particles are much denser and coarser in the as-cast microstructure. According to the XRD patterns (Fig. 2), these particles consist of Mg and Zr phases but no Mg−Yb peaks are observed due to a trace amount of Yb addition. The EDS−SEM point and line analysis (Fig. 3, Points *A*, *B* and Lines *A*, *B*) further demonstrate that the large compounds are rich in Mg and Zr but lean in Yb, which suggests that Yb may be almost dissolved in the Mg matrix and an increase in addition of Zr results in the dominance and coarsening of Zr-rich particles.

3.2 Electrochemical polarization behavior

3.2.1 Potentiodynamic polarization

The potentiodynamic polarization curves of as-cast Mg−1.0Yb alloys with different Zr additions are shown in Fig. 4(a). It is evident that with increasing Zr alloying content, the φ_{corr} shifts to more positive values, which implies that the electrochemical reaction is more difficult, and thus the matrix is less susceptible to corrosion. However, the J_{corr} values, as listed in Table 2, show some fluctuation with increasing Zr addition rather than a monotonic decrease expected. In the Zr-free Mg−1.0Yb alloy, a J_{corr} value of 225 μA/cm^2 was observed, while with a trace amount of 0.2 Zr addition, a sharply increased J_{corr} of 375 μA/cm^2 was obtained. When further increasing the Zr addition to 1.0 and 1.5 wt.%, the lowest J_{corr} of 166 μA/cm^2 followed by a considerably increased value of 277 μA/cm^2 was achieved.

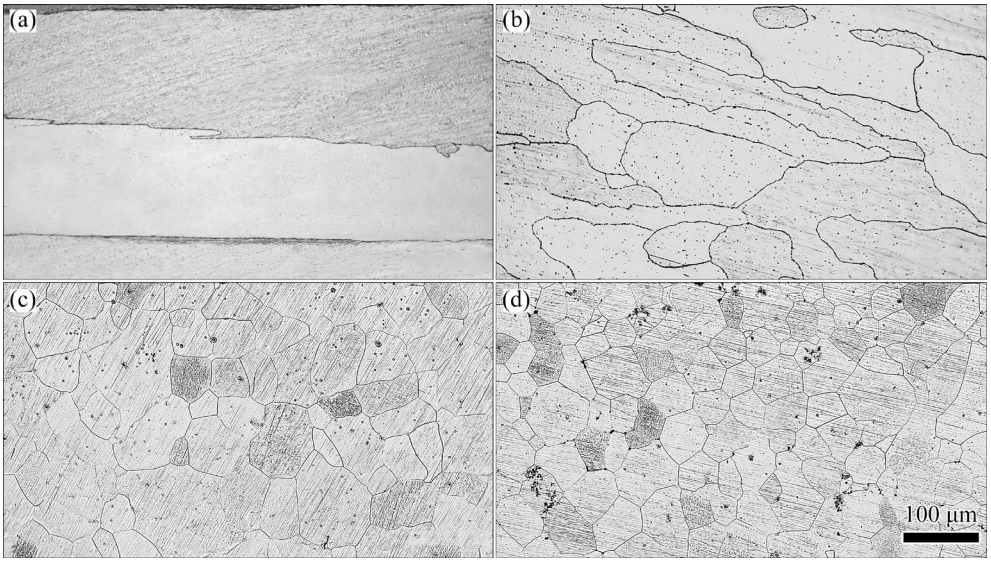

Fig. 1 Optical micrographs of as-cast Mg−1.0Yb−*x*Zr alloys: (a) *x*=0; (b) *x*=0.2; (c) *x*=1.0; (d) *x*=1.5

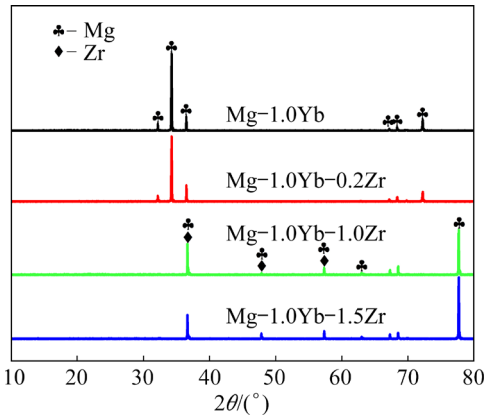

Fig. 2 XRD patterns of as-cast Mg−1.0Yb−*x*Zr alloys

Generally, the magnitude of the corrosion current density is regarded as an indicator of the corrosion rate. The fluctuation in the corrosion current density with the increase of Zr addition indicated that the alloying content of Zr played an important role in the polarization response, which may affect the corresponding corrosion behavior. A trace addition of Zr greatly deteriorated the corrosion resistance of Mg−1.0Yb base alloy, which was similar to the effect with a heavy Zr alloying, but when a proper content of 1.0 Zr was incorporated, the corrosion resistance tended to be improved. Moreover, it was interesting to find that a

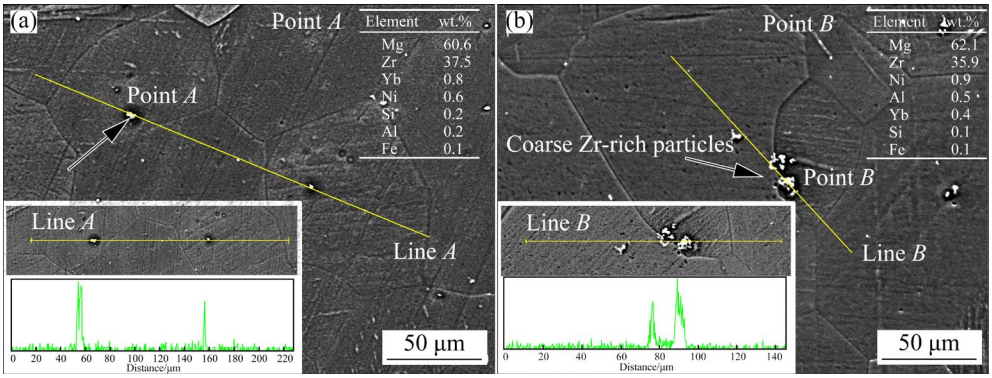

Fig. 3 SEM images and EDS line and point detection results of 1.0 Zr (a) and 1.5 Zr (b) samples

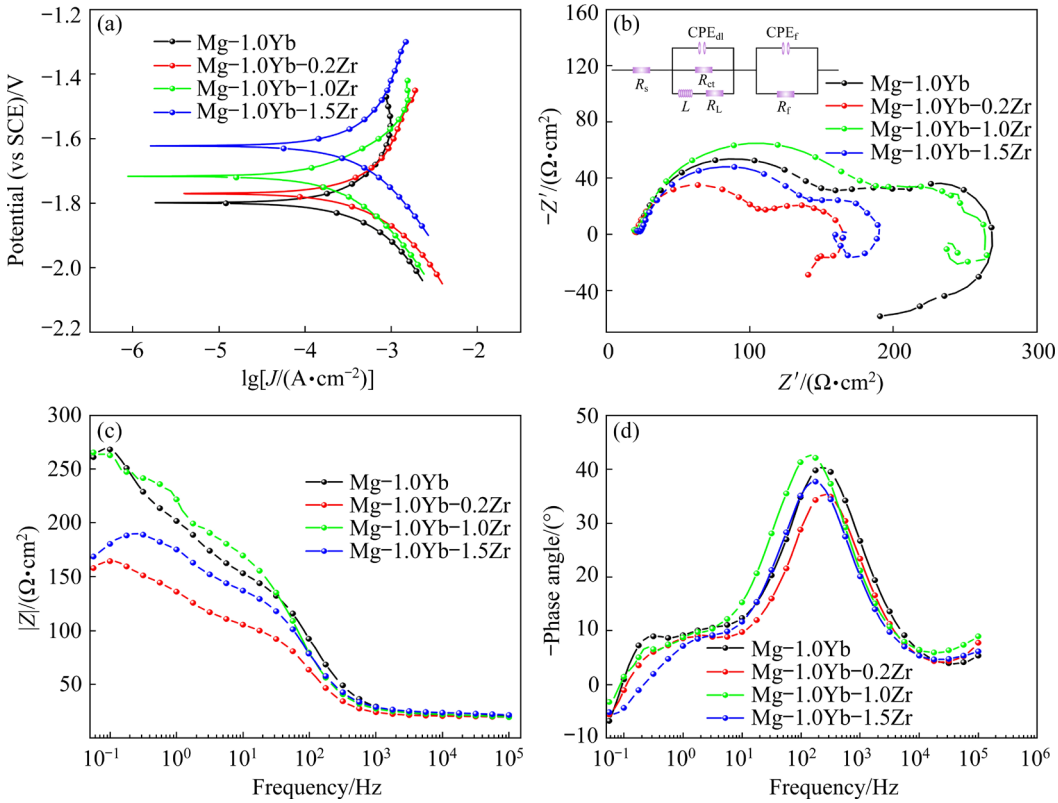

Fig. 4 Potentiodynamic polarization curves (a), Nyquist plots (b), Bode impedance plots (c), and Bode phase angle plots (d) of Mg−1.0Yb−*x*Zr alloys after 6 h immersion in SBF solution

relatively high corrosion current density of 277 μA/cm^2 along with the noblest corrosion potential of −1.622 V (vs SCE) was obtained in the Mg−1.0Yb−1.5Zr sample. The increase in φ_{corr} and J_{corr} may be related to the enhancement of the cathodic reaction rate, resulting from the presence of a nobler phase providing surfaces for a faster cathodic reaction.

3.2.2 EIS data

The EIS plots of the tested alloys measured in SBF solution are depicted in Fig. 4(b). It is evident that the Nyquist plots curves of alloys with different Zr contents show similar characteristics, i.e. two capacitance loops respectively appear in the high-frequency and intermediate-frequency regions along with one inductive loop in the low-frequency region, although it is suppressed to some extent. Generally, a well-established inductive loop at low frequencies implies the relaxation of coverage due to the adsorption of species and pit formation. In this sense, a similar electrochemical corrosion mechanism was observed in all tested alloys during the EIS measurement after 6 h of immersion. Moreover, the diameter of the high-frequency capacitive loop was usually regarded as an indicator of the charge transfer resistance, which meant that a larger diameter corresponded to better corrosion resistance. Accordingly, the degradation rate of the samples decreased in the following order of 0.2 Zr > 1.5 Zr > 0 Zr > 1.0 Zr, which was well consistent with the features that Bode impedance (Fig. 4(c)) and Bode phase angle (Fig. 4(d)) plots presented.

For a better understanding of the EIS impedance results, the equivalent circuits and the fitting data of the EIS spectra are illustrated in Fig. 4(b) and Table 3. R_s, R_{ct}, and R_f represent solution resistance, charge transfer resistance, and film resistance, respectively [22]. In this work, constant phase element (CPE) was employed to compensate for the surface inhomogeneity, resulting from Zr-rich particles, scratches, and oxide films [23]. CPE_{dl} represents the double-layer capacitance in parallel with R_{ct}, while CPE_f represents the constant phase element in parallel with R_f [23]. With increasing Zr contents from 0 to 1.5 wt.%, the values of R_{ct} and R_f decreased firstly and then increased followed by a further decline, in companion with a reverse trend for the values of CPE_f and CPE_{dl}. The results demonstrated that the corrosion resistance for the Mg−Yb−Zr alloy was Zr content dependent, which was well agreed with the polarization results.

3.3 Immersion test results

3.3.1 pH value

The pH variation of the tested alloys immersed in SBF at 37 °C for 120 h is depicted in Fig. 5. It is evident that all the curves develop a continuous rise followed by a plateau, although the durations for reaching stabilization and the final stable pH values

Table 2 Electrochemical parameters derived from potentiodynamic polarization curves of investigated alloys immersed in SBF solution at 37 °C for 6 h

Sample	φ_{corr} (vs SCE)/V	β_a/(mV·decade^{-1})	$-\beta_c$/(mV·decade^{-1})	R_p/(Ω·cm^2)	J_{corr}/(μA·cm^{-2})	η_{corr}/(mm·a^{-1})
0 Zr	−1.798	227	193	202	225	5.14
0.2 Zr	−1.769	379	209	156	375	8.57
1.0 Zr	−1.716	172	216	251	166	3.79
1.5 Zr	−1.622	365	185	193	277	6.32

Table 3 Electrochemical parameters of tested alloys fitted from experimental EIS data after immersion in SBF solution at 37 °C for 6 h

Sample	R_s/(Ω·cm^2)	R_f/(Ω·cm^2)	CPE_f/(Ω^{-1}·cm^2·s^n)	n_1	R_{ct}/(Ω·cm^2)	CPE_{dl}/(Ω^{-1}·cm^2·s^n)	n_2	R_L/(Ω·cm^2)	L/(H·cm^2)
0 Zr	21.48	137.71	3.44×10^{-3}	0.69	130.03	4.12×10^{-5}	0.85	40.28	1150
0.2 Zr	20.49	95.87	5.28×10^{-3}	0.58	77.16	4.10×10^{-5}	0.89	56.59	446
1.0 Zr	20.91	194.42	3.45×10^{-3}	0.46	120.92	3.75×10^{-5}	0.93	46.66	807
1.5 Zr	21.24	161.22	3.52×10^{-3}	0.41	78.13	2.99×10^{-5}	0.99	156.42	156

n, n_1 and n_2 are dispersion indexes; R_L and L are resistance and inductance, respectively

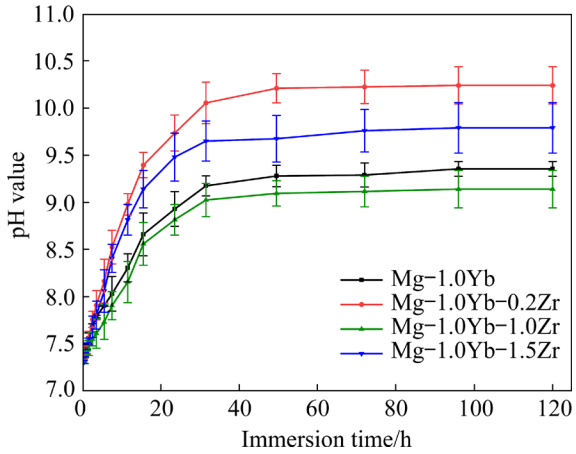

Fig. 5 pH evolution of tested alloys immersed in SBF solution at 37 °C for 120 h

are distinctly different. The Zr-free and 1.0 Zr samples exhibited lower pH values and slower rising rates than 0.2 Zr and 1.5 Zr counterparts during immersion, suggesting a slightly weaker alkalization reaction resulting in a slower equilibrium process. Since a higher pH value generally indicates a higher corrosion rate, a trace amount or heavy addition of Zr may deteriorate the corrosion resistance of the matrix. On the contrary, a proper alloying content of 1.0 Zr may effectively decline the degradation rate of the Mg−1.0Yb base alloy. These observations are correlated well with the results of electrochemical measurements.

3.3.2 Corrosion rate

Generally, the corrosion rate was used to quantitatively compare the degradation speed and then estimate the corrosion resistance of the samples. In this work, the corrosion rate was calculated by the mass loss to comprehensively consider the effects of hydrogen evolution, corrosion-productive film, micro-galvanic corrosion, and the long-term corrosion profile. The temporal evolution of bulk erosion for Mg−1.0Yb alloy with different Zr additions is depicted in Fig. 6. During 720 h immersion, the order of corrosion rates for all the alloys was not changed, with the following increasing order: 1.0 Zr < 0 Zr < 1.5 Zr < 0.2 Zr. The corrosion rates of 0.2 Zr and 1.5 Zr samples were much larger than those of 0 Zr and 1.0 Zr counterparts. Moreover, a very similar evolutionary history was observed in the latter two samples, suggesting that the identical corrosion mechanism may be in control. As evident in Fig. 6, the corrosion rates of 0 Zr and 1.0 Zr alloys almost maintain steadily after exposure to SBF for 168 h. On the contrary, after a steep decline during the first 168 h immersion, the corrosion rates for 0.2 Zr and 1.5 Zr samples increased rapidly followed by a complete dissolution after exposure to SBF for 240 h.

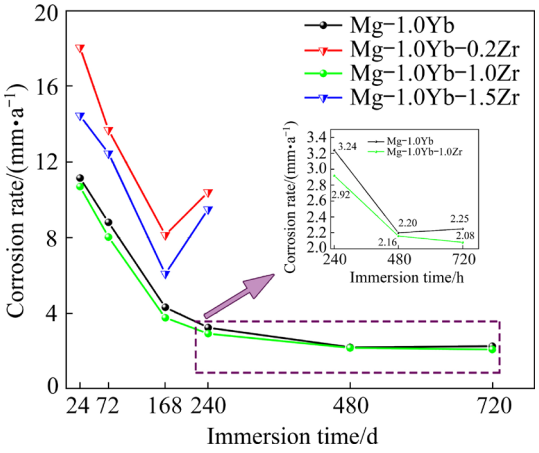

Fig. 6 Corrosion rate curves of Mg−1.0Yb−*x*Zr alloys immersed in SBF solution at 37 °C for different time

The rise in the corrosion rate after a relatively long immersion was probably due to the breakdown of the protective corrosion layer. The available study indicated that the corrosion rate was intimately correlated with the deteriorative effect resulting from micro-galvanic corrosion and the protective effect rooted in the formation of a passivation layer on the corroded surface. In the case of the 0.2 Zr sample, the ability to resist local breakdown in the protective film was very weak and the corrosion behavior may be dominated by the micro-galvanic corrosion induced by its initial heterogeneous grain structure with large discrepancies in grain size and morphology (c.f. Fig. 1(b)). While in the heavily alloyed 1.5 Zr sample, the excessive Zr alloying could stabilize the film to some extent and thus improve homogenous corrosion, but the prevalence of coarse Zr-rich intermetallics accelerated the micro-galvanic corrosion, promoting the breaking down of the protective layer due to the attack of aggressive ion such as chloride. Accordingly, the occurrence of rapid destruction in 0.2 Zr and 1.5 Zr samples after 240 h of immersion was observed.

3.3.3 Surface corrosion morphologies

Figure 7 presents the surface characteristics of the corroded regions of the tested samples before and after removal of the corrosion products after

exposure to SBF solution for 24 and 240 h, respectively. Obviously, the corrosion severity varied with different Zr additions and aggravated with extended immersion time. The 0 Zr and 1.0 Zr samples exhibit better surface quality than the 0.2 Zr and 1.5 Zr counterparts, i.e. although tiny cracks resulted from dehydration appear on their surfaces, a relatively compact and intact corrosion layer is developed and no evident localized corrosion is observed (Figs. 7(a) and (e)), suggesting that the general corrosion dominates the degradation process in the 0 Zr and 1.0 Zr samples. By contrast, a lot of large and deep pits cover the corroded surface of the 0.2 Zr sample (Fig. 7(c)), indicating that much severe corrosion attack occurs. The detailed investigation further manifested that a large amount of corrosion products peeled off along grain boundaries, so it was speculated that the initial heterogeneous grain structure with large discrepancies in grain size and morphology resulted in a rapid local deterioration (c.f. Fig. 1(b)).

In the case of 1.5 Zr alloy (Fig. 7(g)), a thick corrosion layer with wider cracks was observed after 24 h immersion. After removing the corrosion products (Fig. 7(h)), a rough corroded surface with a high density of corrosion pits was exposed, indicating that a moderate corrosion level was achieved in the 1.5 Zr sample as compared with the 0.2 Zr counterpart. Further, it was interesting to find that two representative corrosion products with distinct SEM contrasts and morphologies dominated the corrosion layer of the 1.5 Zr sample. As the magnified SEM micrographs demonstrated, the upper region marked with Point *A* is covered with grey needle-like compounds. The EDS point detection, as listed in Table 4, indicates that Point *A* is rich in Mg, Cl, and O elements and lean in Ca, P, Zr, and Yb elements. Therefore, the corrosion layer in this region may be primarily composed of $MgO/Mg(OH)_2$ and $MgCO_3$ with some enrichment of Cl^- resulting from either the remaining Cl^- in the SBF solution or the formation of $MgCl_2$ as a reaction product. Due to its loose and fluffy structure, the very film could provide limited corrosion protection and was susceptible to rapid degradation.

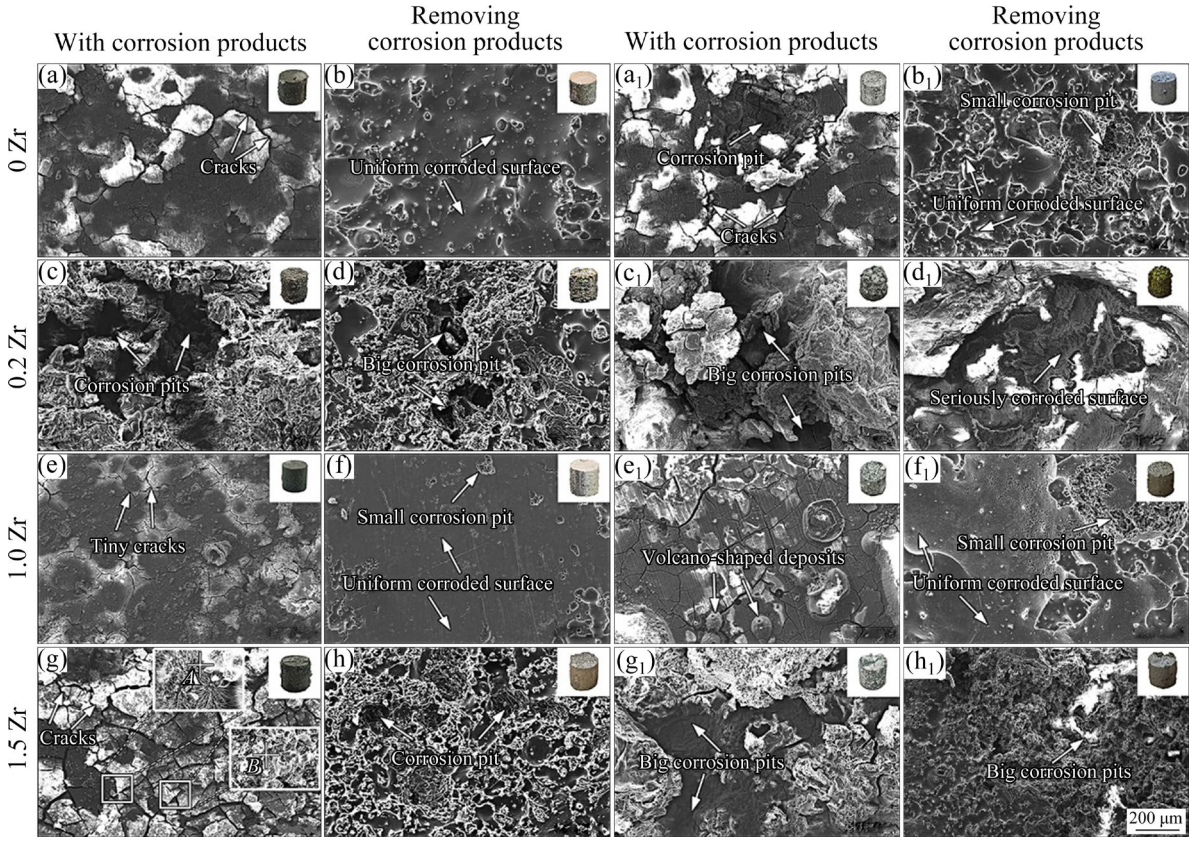

Fig. 7 Scanning electron micrographs of corroded surfaces for Mg−1.0Yb−*x*Zr alloys after immersion in SBF solution at 37 °C for 24 h before (a, c, e, g) and after (b, d, f, h) removal of corrosion products and for 240 h before (a_1, c_1, e_1, g_1) and after (b_1, d_1, f_1, h_1) removal of corrosion products

Table 4 EDS point analysis results of Points *A* and *B* in Fig. 7 (at.%)

Point	O	Mg	P	Ca	Cl	Na	Zr	Yb
A	67.3	24.5	0.5	1.3	4.9	0.9	0.5	0.1
B	59.9	10.6	15.2	10.1	0.2	2.6	0.8	0.6

By contrast, the corrosion layer displayed in the right region is much dense and compact, with a brighter contrast in the SEM image. The EDS point analysis (Table 4) reveals that Point *B* has lower amounts of Mg, Cl, and O elements and higher contents of Ca, P, Zr, and Yb elements than Point *A*. The white products can be related to the formation of $Mg(OH)_2$ and Ca−P compounds. It was speculated that the initially developed $Mg(OH)_2$-rich corrosion outer layer generated by a dissolution−precipitation mechanism [24] may partly react with the abundant Cl^- in the SBF solution, thus generating the soluble $MgCl_2$ compound. With advancing corrosion, Ca and P in the electrolyte deposited on the corrosion layer rich in $Mg(OH)_2$. As a larger diffusion rate of phosphates compared to calcium ions in the corrosion layer, $Mg_3(PO_4)_2$ developed first with $Mg(OH)_2$ acting as a precipitation nucleus, followed by a replacement of Mg^{2+} by Ca^{2+} and then $Ca_3(PO_4)_2$ formed. Due to the nature of thermodynamically stable compounds (small solubility product), $Mg_3(PO_4)_2$ and $Ca_3(PO_4)_2$ were the final conversion products of the initial $Mg(OH)_2$ layer (the substitution mechanism) [25−27]. Moreover, higher contents of Zr and Yb elements in this region possibly further stabilized the corrosion layer. Due to its compact structure and thermodynamically stable nature, this conversion layer could provide better corrosion protection from the rapid destruction of the local region.

While in the case of 1.0 Zr sample, it is interesting to find that the volcano-shaped structures are still observable after exposure to SBF solution for 240 h (Fig. 7(e_1)). The presence of the volcano-like deposit was an indicator of the vigorous hydrogen evolution from the cathodic intermetallics beneath it, originating from the water reduction due to localized micro-galvanic corrosion with the anodic Mg matrix. The hydrogen evolution is correlated with the release of hydroxide ions, i.e. the development of a local alkaline environment [26]. Available research reported that the impurities in the melt would co-precipitate with Zr and form a Zr-rich cathodic center during erosion, which may play an essential role in the development of the volcano-shaped structure. Moreover, with increasing distance from the cathodic center, a homogeneous but clod-like corrosion layer is visible on the external surface, which should result from drying during sample preparation. This uniformly growing corrosion layer on the 1.0 Zr corroded surface was inclined to cover these volcano-shaped deposits, thus weakening the cathodic reaction and suppressing mass transport across the corrosion layer after an extended immersion duration. Accordingly, a protective corrosion layer was developed and the slightest corrosion attack was observed in the 1.0 Zr alloy.

3.3.4 Cross-sectional corrosion morphologies

Figures 8 and 9 exhibit the cross-sectional SEM micrographs and the corresponding EDS mappings of the samples after exposure to SBF solution for 24 and 240 h, respectively. Different types of corrosion layer build-up are discerned for the alloys with different Zr additions. The corrosion layers on 0 Zr and 1.0 Zr samples are homogeneous and compact while a heterogeneous and porous corrosion layer with visible wide cracks developed on the 0.2 Zr and 1.5 Zr counterparts, especially for the 0.2 Zr sample. It is obvious that a deep corrosion pit almost penetrates the entire corrosion product region into the bulk (Fig. 8(b)), indicating the prevalence of severe corrosion attacks and rapid local degradation. To precisely characterize and compare the matrix erosion, the pitting factor which is defined as the ratio of the deepest pit depth to the average penetration, is calculated and listed in Table 5. Consistently, the 0 Zr and 1.0 Zr samples characterized lower pitting factors (1.28 and 1.08) compared with those of 0.2 Zr and 1.5 Zr counterparts (2.97 and 2.87), revealing the former tended to more uniform localized corrosion. The latter, especially for the 0.2 Zr sample in contrast exhibited deeper corrosive metal penetration, suggesting that severe degradation occurred and un-uniform corrosion dominated.

Regarding the distribution of the elements, the corrosion products of the samples mainly contained Mg and O elements, indicating the dominance of $MgO/Mg(OH)_2$ compounds. At initial corrosion (immersion for 24 h), different element distributions are observed in the samples with a trace and sufficient

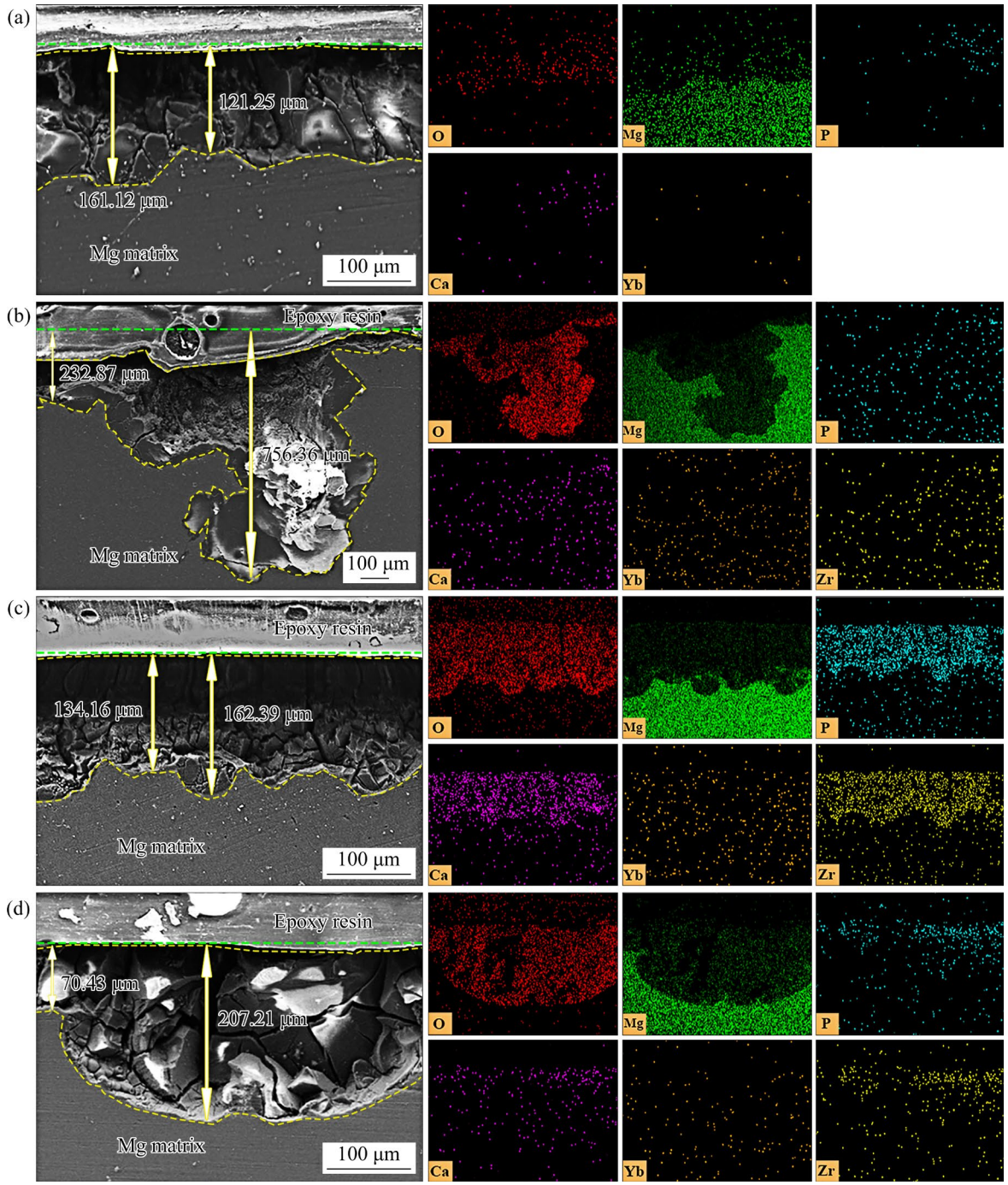

Fig. 8 Cross-sectional SEM images and corresponding EDS patterns of alloys with different Zr contents immersed in SBF solution at 37 °C for 24 h: (a) 0 Zr; (b) 0.2 Zr; (c) 1.0 Zr; (d) 1.5 Zr

amount of Zr alloying samples (c.f. Fig. 8). In the cases of 1.0 Zr and 1.5 Zr samples, a pronounced P and Ca elements co-existed with Zr in the product layers, but no such a strong distribution-pattern was observed in the cases of 0 Zr and 0.2 Zr counterparts. This phenomenon can be reasonably explained by the powerful affinity between Zr and phosphate [28,29]. In other words, the addition of Zr was in favor of the $Mg_3(PO_4)_2$ precipitation with $Mg(OH)_2$ functioning as the nucleus during the initial degradation, thus promoting the formation of the protective conservation layer rich in $Mg_3(PO_4)_2$ [26]. Due to the operation of the substitution mechanism, the $Ca_3(PO_4)_2$ compound partly developed afterward, and that was why the co-existence of Ca element was in the same layer [30].

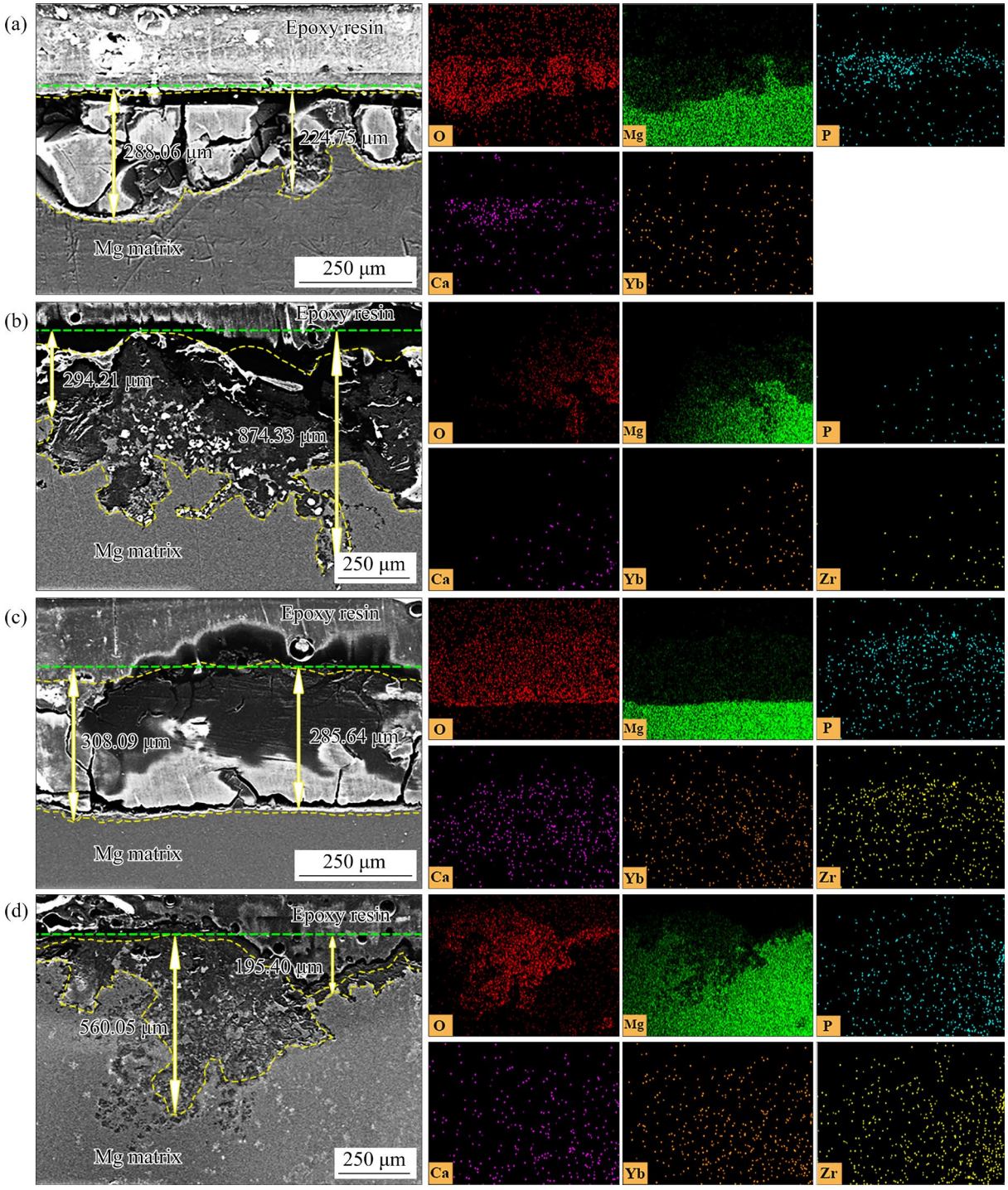

Fig. 9 Cross-sectional SEM images and corresponding EDS patterns of alloys with different Zr contents immersed in SBF solution at 37 °C for 240 h: (a) 0 Zr; (b) 0.2 Zr; (c) 1.0 Zr; (d) 1.5 Zr

Table 5 Pitting factors of alloys with different Zr additions after immersion in SBF solution at 37 °C for 24 and 240 h

Immersion time/h	Pitting factor			
	0 Zr	0.2 Zr	1.0 Zr	1.5 Zr
24	1.33	3.25	1.21	2.94
240	1.28	2.97	1.08	2.87

After exposure to SBF solution for 240 h, the precipitation of Ca and P is slightly distinct for the Zr-free sample (Fig. 9(a)), suggesting the slow formation of P−Ca compounds, which in contrast further confirms the promotion effect of Zr in $Mg_3(PO_4)_2$ precipitation. Additionally, the element distribution of the severely corroded 0.2 Zr sample (Fig. 9(b)) seems much sparser than that of other

samples, which is due to the loose nature of the corrosion product and much of them may be stripped off during sample preparation. For the 1.0 Zr sample (Fig. 9(c)), the elemental distribution after 240 h of immersion remains similar to that observed after 24 h. Moreover, the distribution of P, Ca, and Zr elements in the corrosion layer is distinguishable. The XPS and XRD analysis results as shown in Fig. 10 also demonstrate the dominance of $Mg(OH)_2$ and the presence of phosphates in the corrosion products. In addition, it was worth noting that the distribution of Yb is fairly uniform both in the corrosion product and the Mg matrix irrespective of the Zr content and immersion time. This phenomenon revealed that Yb was mostly dissolved in the matrix and the role of Yb in these Zr-containing alloys is stabilizing the corrosion layer and matrix, which rules out the possibility of Yb-containing intermetallics acting as the cathodic particle in this alloy system.

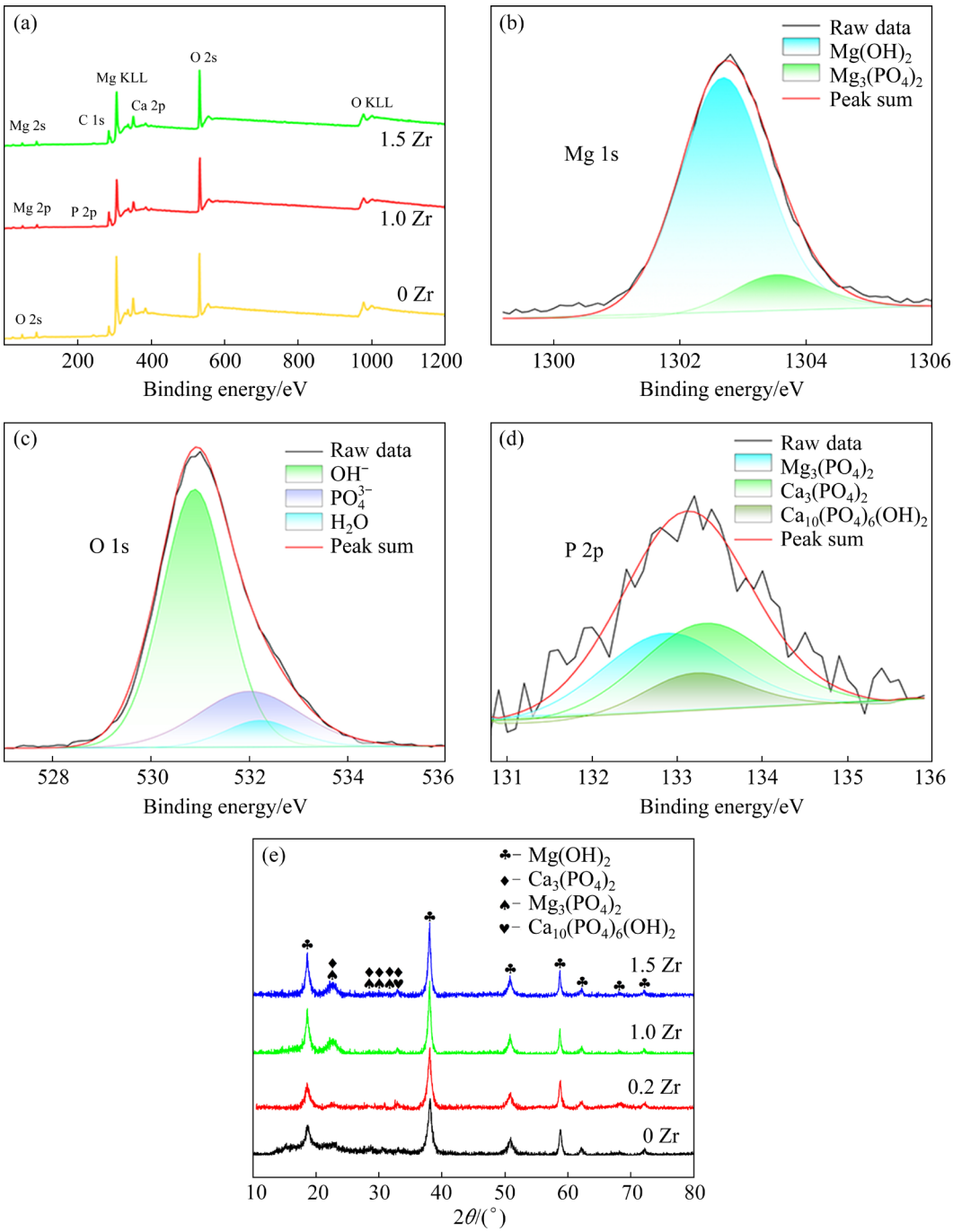

Fig. 10 XPS survey spectra of Mg−1.0Yb−*x*Zr alloys (a), high-resolution XPS spectra for Mg 1s (b), O 1s (c), P 2p (d) of corrosion products on surface of 1.0 Zr sample, and XRD patterns (e) of corrosion products of different samples

3.4 Mechanical properties and fracture characteristics

The tensile yield strength (TYS), ultimate tensile strength (UTS), and elongation to fracture (EL) are listed in Table 6. Obviously, the Zr addition exerts beneficial effects on the tensile properties of the Yb-containing Mg alloys. According to the fractographic examination as shown in Fig. 11, all the as-cast samples exhibit a typical brittle fracture mode with large cleavage planes and tear ridges despite some small dimples occasionally observed in the cases of 1.0 Zr and 1.5 Zr samples.

Table 6 Tensile properties of different samples

Sample	UTS/MPa	TYS/MPa	EL/%
0 Zr	85±1.7	29±1.6	4.8±1.2
0.2 Zr	104±2.2	35±1.1	6.1±1.1
1.0 Zr	142±2.5	53±1.9	9.8±0.9
1.5 Zr	147±1.9	89±1.6	7.6±1.3

3.5 Cytocompatibility and hemocompatibility

The aforementioned investigations demonstrated that the 1.0 Zr sample possessed a good combination of corrosion resistance and mechanical properties. In this section, the biocompatibility of this alloy was evaluated by cytocompatibility and hemocompatibility in vitro. The heavily alloyed 1.5 Zr sample was adopted for comparison. Figures 12(a) and (b) depict the cell viability of the 1.0 Zr and 1.5 Zr samples after being cultured in 10% extract for 24 and 72 h, respectively. Evidently, the cell viability for the two samples was about 100% for 24 h of cultivation, and even a slight increase was observed after 72 h, indicating that both alloys have favorable good cell compatibility according to ISO 10993−5:1999 standard. In addition, the 1.0 Zr alloy showed a higher cell survival rate, suggesting the enhanced corrosion resistance suppressing the release of the OH^- ions, thus in favor of the maintenance and growth of cells. Notably, Fig. 12(c) indicates that both samples have good hemocompatibility with the hemolysis rates lower than the safe line of 5% according to ISO 10993−4:2002, especially for the 1.0 Zr alloy presenting a low hemolysis rate of 2.169%. The above-mentioned in-vitro tests demonstrated that the studied alloy may have favorable biocompatibility and the 1.0 Zr alloy can be a potential candidate for biomedical applications.

4 Discussion

4.1 Effect of Zr addition on microstructure and corrosion of Mg−1.0 Yb alloy

Zr has a potent growth restriction effect on Mg grains during solidification (growth restriction

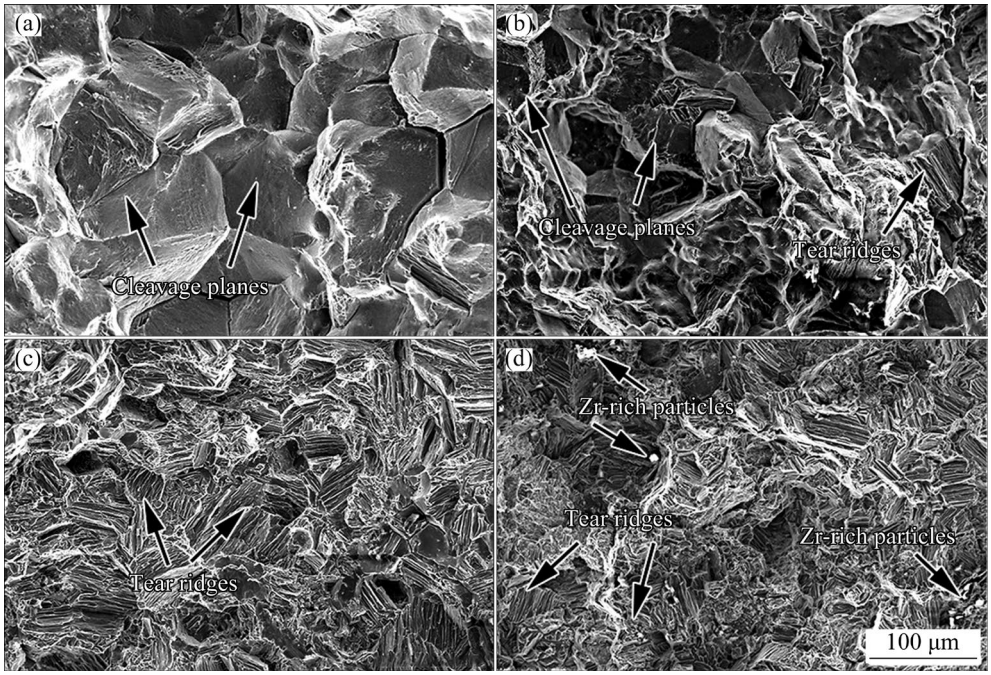

Fig. 11 SEM images of tensile fracture surfaces of different samples: (a) 0 Zr; (b) 0.2 Zr; (c) 1.0 Zr; (d) 1.5 Zr

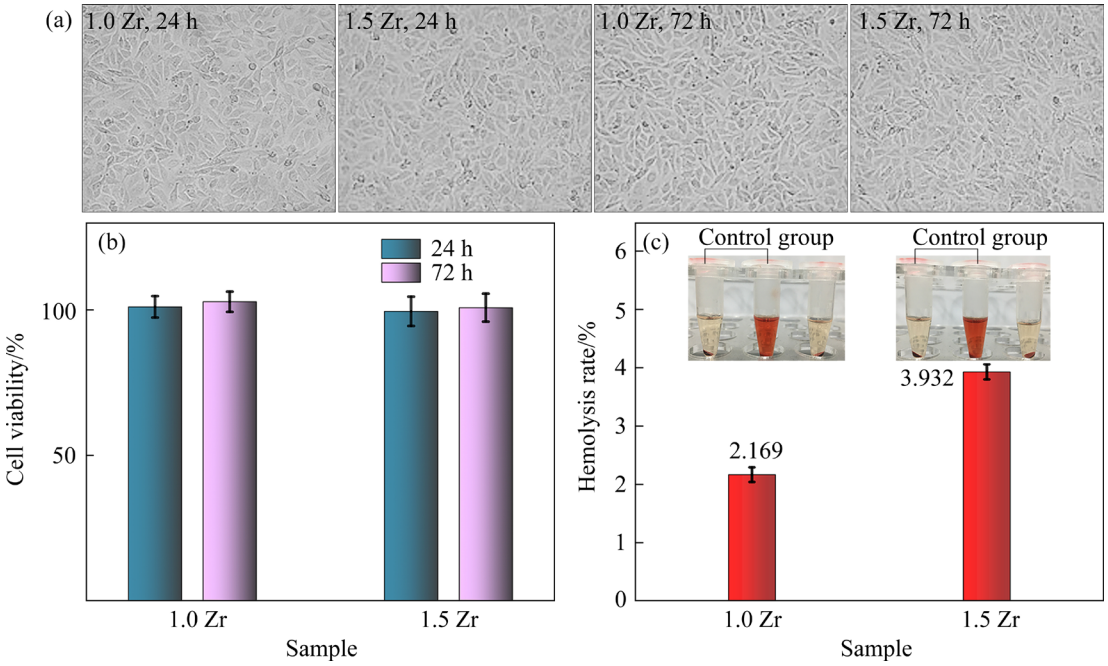

Fig. 12 Cell states after 24 and 72 h incubation (a), cell viability histogram (b), and hemolysis rate (c) for tested samples (Erythrocytes in DI water and PBS served as positive and negative controls, respectively)

factor, GRF=38.29). Combined with heterogeneous nucleation, a fine equiaxed grain structure can be finally developed, resulting in a significant improvement in mechanical properties. On the other hand, Zr exhibits efficacy in precipitating impurities such as Fe, Ni, Al, and Si from the melt, thus purifying the melt and elevating the corrosion resistance of the alloy [31]. As a result, adding an appropriate amount of Zr to the Mg melt has been widely recognized as a viable strategy for refining the grain size and purifying the melt in as-cast Mg alloys. However, the question of the optimal content of Zr that would confer benefits in mechanical properties enhancement without compromising corrosion performance, in the context of a specific alloy composition, remains a matter of ongoing debate. In particular, the study of the effect of Zr addition on the microstructure and comprehensive properties of Mg alloys that contain trace amounts of Yb has not yet been reported.

In this work, four types of Mg−1.0Yb alloys with different Zr contents were prepared, corresponding to the alloy compositions of Zr-free, a trace, slightly excessive, and excessive Zr additions, and the effect of Zr addition on the microstructure and mechanical properties of the as-cast Mg−1.0Yb alloy was systematically investigated. The results indicated that with increasing Zr contents, the as-cast grains of the alloy changed from the typical columnar shape (0 Zr) and the mixed grain structures with columnar along with equiaxed grains (0.2 Zr) to the fully equiaxed coarse grains (1.0 Zr), and finally the fine equiaxed grain structures (1.5 Zr). This demonstrated that the addition of Zr can significantly change the morphology and size of the as-cast Mg−1.0Yb alloy grains and that the grain morphology was more sensitive to Zr addition. It may be related to the preferential heterogeneous nucleation of the Mg grains surrounding Zr particles which possessed a high melting point and low diffusion rate in the Yb-containing supercooled melt. As the equilibrium partition coefficient (k) of Yb in Mg is less than 1 ($k \approx 0.17$), Yb atoms tend to segregate at the solid−liquid interface, resulting in supercooling of the melt, which is also the reason why the as-cast grain of 0 Zr alloy is smaller than that of pure Mg [16].

When a small amount of Zr was incorporated into the supercooled Mg−1.0Yb melt, due to a higher solute concentration at the solid−liquid interface, the alloy tended to heterogeneously nucleate with Zr in the melt, so that the original coarse dendrites were divided and grew without preferential directions, thus gradually becoming equiaxed. Actually, this effect is not so significant

in the 0.2 Zr alloy due to the trace addition of Zr as depicted in Fig. 1(b). However, when the Zr content increased to 1.0 wt.%, a fully equiaxed grain structure was achieved and the microstructure tended to be uniform. Furthermore, the equiaxed grains were further refined in companion with the coarsening of Zr-rich particles when the Zr content increased to 1.5 wt.%, which was greatly in favor of the strength improvement. These phenomena indicated that Zr addition can promote the equalization and refinement of as-cast grains of Yb-containing Mg alloys, but this modification potential can be fully realized with a sufficient amount of Zr addition.

In regard to corrosion behavior, it should first be emphasized that the matrix material studied in this work was pure Mg with dilute Yb element addition. According to the phase diagram, the solubility of Yb in Mg is 3.3 wt.% (at the eutectic temperature of 500 °C), and Yb does not form a compound with Zr. Therefore, 1.0 wt.% Yb can be completely dissolved in the Mg matrix, which rules out the possibility of severe local corrosion caused by Yb-containing cathode particles. According to our previous study [14], Yb solute in Mg predominantly played a beneficial role in stabilizing the protective film during corrosion, which may be the main reason why the Zr-free Mg−1.0Yb alloy generally possessed desirable corrosion resistance. With increasing Zr content, the corrosion potential became nobler due to a higher standard electrode potential of Zr (−1.53 V) relative to Mg (−2.37 V), which suggested that the corrosion resistance of the alloy was improved with increasing Zr addition from the thermodynamic point of view. However, the immersion experiment indicated that the corrosion rate of the alloy varied with Zr additions and immersion time (as shown in Fig. 6), and there were two different degradation tendencies, i.e. the uniform corrosion and the galvanic corrosion (as shown in Fig. 7).

Specifically, when a trace amount of 0.2 wt.% Zr was added, the corrosion resistance of the alloy degraded sharply. The marked deterioration of corrosion resistance was rooted in the initial heterogeneous grain structure in terms of grain size and morphology of as-cast grains caused by a trace amount of Zr addition, which may lead to the potential difference between the large columnar and fine equiaxed grains and thus the formation of micro-galvanic couple accelerating the destruction of protective corrosion film. ZENG et al [32] also reported a similar phenomenon for the micro-galvanic corrosion between the two distinct layers of an extruded ZK60 bumper with an initial potential difference. In addition, when the addition of Zr was increased to 1.5 wt.%, the micro-galvanic corrosion caused by the coarsening of Zr-rich particles dominated the corrosion mode of the alloy. The difference in local degradation rate generated a corrosion layer where loose $Mg(OH)_2$. coexisted with compact Ca−P compounds. This facilitated the rapid penetration of Cl^- ions into the substrate through the porous $Mg(OH)_2$ and $MgCl_2$ layers, ultimately leading to the development of large corrosion pits that penetrated the corrosion products (Fig. 8). In this process, the corrosion shield of fine particles distributed at grain boundaries as well as the stabilizing effect of Zr and Yb on the film may provide some positive effects in inhibiting rapid localized corrosion, but they lose the predominant role in the competition with the accelerated cathode reaction triggered by the coarsening of Zr-rich particles, and finally developed a corrosion mechanism with the coexistence of dense passive film and deep corrosion pits on the corroded surface of 1.5 Zr alloy. The results revealed that an excessive Zr addition was detrimental to the overall corrosion resistance of the Mg−1.0Yb alloy.

In contrast, the corrosion resistance of the alloy was significantly improved with a 1.0 wt.% Zr addition. Electrochemical tests, metallographic examination, corrosion surface morphology, and corrosion cross-section observations demonstrated that the improvement of corrosion resistance was mainly attributed to the following positive effects induced by sufficient Zr addition. Firstly, a fully equiaxed as-cast grain structure with relatively uniform grain size was achieved, the initial potential difference was alleviated and thus severe local corrosion was prevented. Secondly, the adsorption of Zr on phosphate was increased to promote the $Mg_3(PO_4)_2$ precipitation with $Mg(OH)_2$ acting as the nucleus, which resulted in the development of a more thermodynamically stable compact layer. Thirdly, the dispersed distribution of the fine Zr-rich particles was beneficial to the formation of continuous corrosion products film, which made the alloy tend to be uniformly corroded. Lastly, a sufficient Zr solute combined with almost

dissolved Yb in the matrix further improved the stability and adhesion of the corrosion film. The corrosion mechanisms of the tested alloys are schematically demonstrated in Fig. 13.

Furthermore, it was worth mentioning that the degradation rate and corrosion morphology of 0 Zr and 1.0 Zr alloys were very similar after exposure to SBF solution during 480 h, but advancing immersion, the corrosion resistance of Zr-containing alloy was slightly better than that of Mg−Yb matrix (Figs. 6 and 7). This phenomenon may be due to the adhesion improvement between the product film and the substrate after Zr addition, prolonging the long-term stability of the protective layer in corrosive media. Actually, a trace or excessive addition of Zr degraded the corrosion resistance of Mg−Yb alloy in SBF solution, although the mechanical properties improved to some extent. An appropriate amount of Zr addition (1.0 wt.% in this study) can synergistically improve strength and ductility without sacrificing the initial excellent corrosion resistance of the Mg−1.0Yb cast alloy.

4.2 Effect of Zr addition on mechanical properties of Mg−1.0Yb alloy

Table 6 indicates that the tensile properties of the Mg−1.0Yb cast alloy are Zr-content dependent. With increasing Zr additions, the TYS increased continuously from ~29 MPa in the case of the 0 Zr sample to ~35, ~53, and ~89 MPa in the cases of 0.2 Zr, 1.0 Zr, and 1.5 Zr samples, respectively. In regard to the ductility, a slightly excessive Zr addition (1.0 wt.%) doubled the EL from ~4.8% in the case of Zr-free alloy to ~9.8% in the case of 1.0 Zr counterpart, and contrarily a decline in elongation was observed in the 1.5 Zr tensile sample (~7.6%). The slight deterioration in ductility after a heavy Zr addition was attributed to the presence of coarse Zr-rich particles, which induced the local stress concentration and the occurrence of premature failure. This inference can be verified by the fracture characteristic as illustrated in Fig. 11(d). Evidently, large bright particles are located in irregularly spaced tear ridges.

Figure 14 illustrates the tensile data collected in this study and available records for typical as-cast ternary Mg alloys [33−37]. The results highlighted that the 1.0 Zr sample exhibited good ductility along with moderate tensile strength in comparison with the listed counterparts. With increasing Zr additions, an obvious decrease in grain size from ~219 μm in the Zr-free sample to ~62 and ~54 μm in the cases of 1.0 Zr and 1.5 Zr counterparts was observed, along with the precipitation, dispersion, and then the coarsening of Zr-rich particles (Figs. 1 and 3). The grain refinement and particle precipitation/dispersion should be predominantly responsible for the pronounced improvement in the tensile strength. The observation of the tensile microstructures may

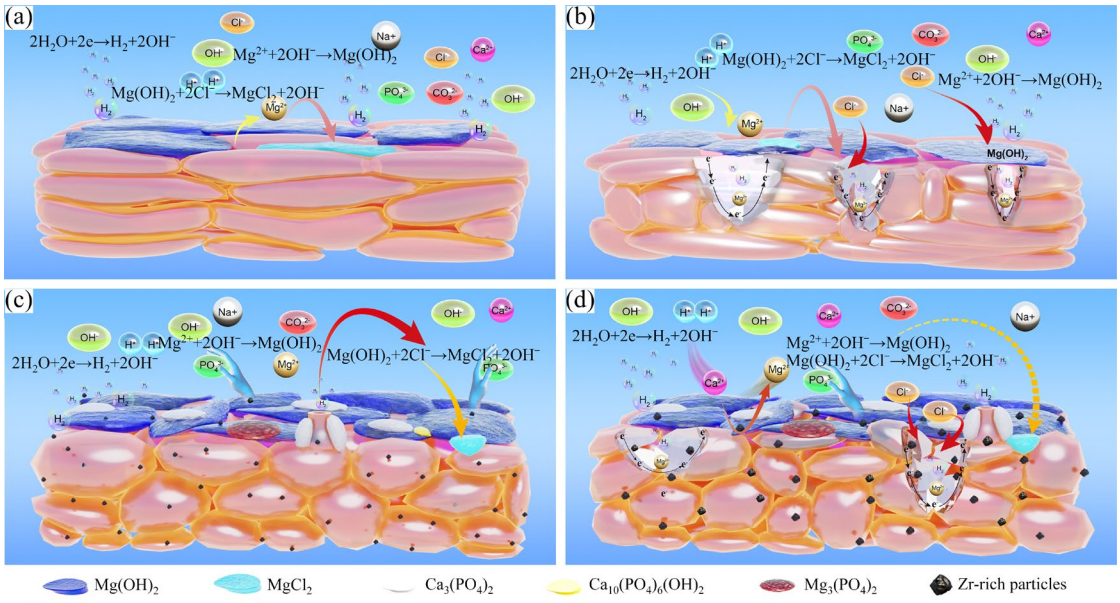

Fig. 13 Schematic diagrams of corrosion mechanisms in different samples: (a) 0 Zr; (b) 0.2 Zr; (c) 1.0 Zr; (d) 1.5 Zr

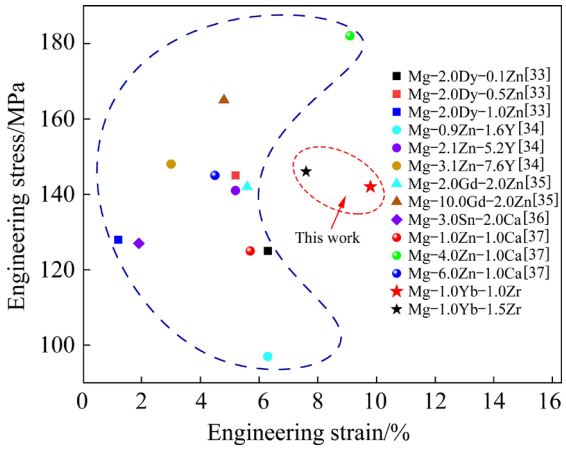

Fig. 14 Comparison of mechanical properties in this work with results reported in literature

provide more direct insight into these effects. Figure 15 depicts the representative orientation maps, grain boundary distribution patterns, and the corresponding basal pole figures of 0.2 Zr and 1.0 Zr alloys after tensile tests. It is found that the extension twin boundaries, as identified in Figs. 15(c) and (f) (corresponding to the 86.3° peaks), are prevalent in the tensile microstructures, suggesting that the extension twinning should be robustly activated during stretching.

With increasing Zr addition from 0.2 to 1.0 wt.%, the area fraction of the twins increased from 12.7% to 30.2% in companion with a transition in twin morphology. Apparently, the aspect ratios of twin dendrites in the 1.0 Zr sample were much smaller and most of the twins traversed the entire grain. In contrast, the twins in 0.2 Zr alloy generally possessed larger aspect ratios but terminated within the grain interior. This phenomenon was resulted from the microstructure developed with a slightly excessive Zr addition. As indicated in Fig. 1, a mixed columnar−equiaxed grain structure in the 0.2 Zr sample is fully transitioned into equiaxed grains in the 1.0 Zr sample, corresponding to more secondary and weaker basal poles in the (0001) pole figure as shown in the inset of Fig. 15(d). The homogeneous equiaxed grain structure with a coarse enough grain size (~62 μm) facilitated the priority development of extension twins during stretching, as the critical resolved shear stress (CRSS) value of extension twinning is very low (~3 MPa). Additionally, the fine Zr-rich particles dispersed in the 1.0 Zr matrix restricted the further growth of the twins. Therefore, profuse extension twins with a smaller aspect ratio were generated in the 1.0 Zr tensile sample. These twin boundaries (TBs) here functioned the same as the high-angle grain boundaries (HAGBs) to impede dislocation migration and promote grain boundary strengthening.

Figure 16 shows kernel average misorientation (KAM) diagrams and in-grain misorientation axes (IGMA) analyses of 0.2 Zr and 1.0 Zr samples. It is well-known that the KAM values account for local

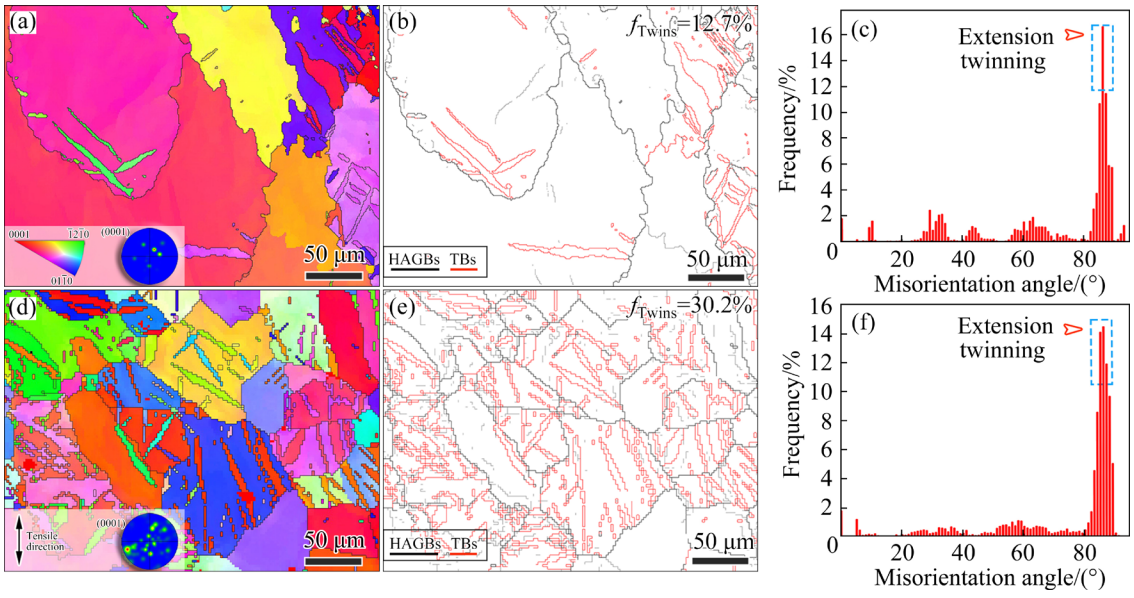

Fig. 15 EBSD orientation maps (a, d), grain boundary maps (b, e), and misorientation distributions (c, f) of 0.2 Zr (a−c) and 1.0 Zr (d−f) samples

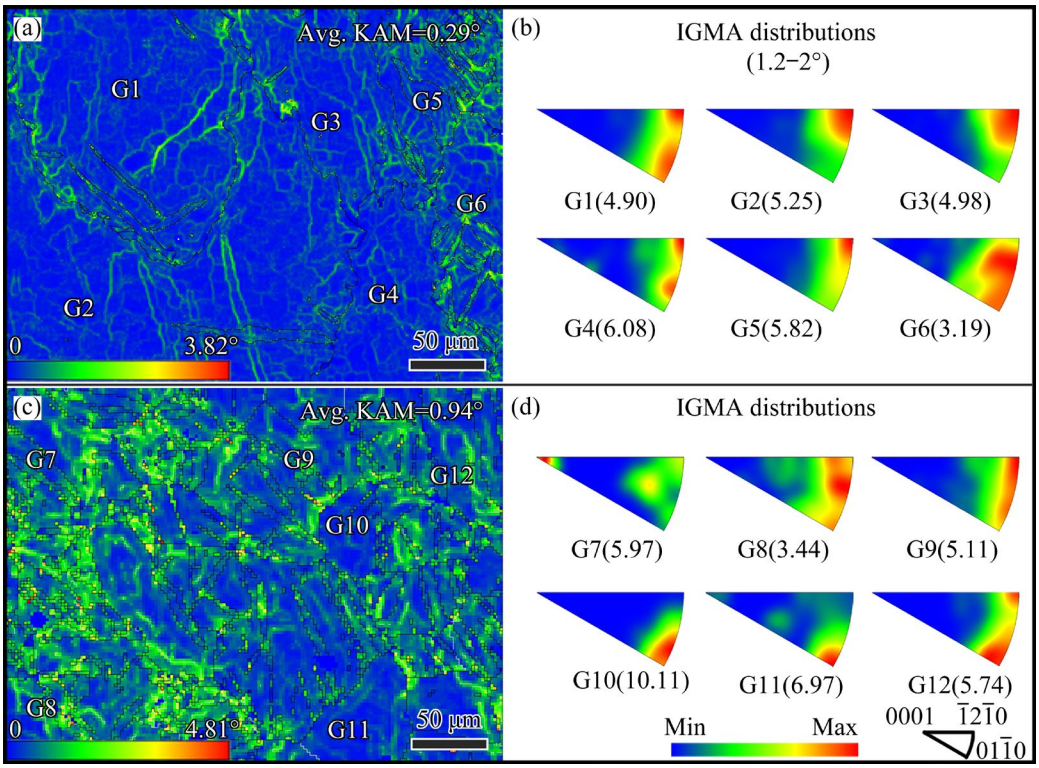

Fig. 16 KAM diagrams (a, c) and IGMA analysis results (b, d) of 0.2 Zr (a, b) and 1.0 Zr (c, d) samples (The value in parenthesis indicating the maximum value of IGMA intensities)

lattice distortion/localized deformation, which is directly proportional to the geometrically necessary dislocation (GND) density [38]. As shown in Figs. 16(a) and (c), the average KAM value of the 1.0 Zr sample is 0.94°, which is much larger than that of the 0.2 Zr counterpart (0.29°), suggesting that a higher level of dislocation density is developed in the 1.0 Zr sample. This phenomenon was correlated with the finer microstructure and larger solute concentration induced by a slight excess of 1.0 wt.% Zr addition, which further improved the strength by grain boundary and solution strengthening.

According to the IGMA analysis theory, the dominant deformation mechanism can be identified by matching the Taylor axis for a given slip mode to the experimentally measured IGMA [39]. Figures 16(b) and (d) depict the IGMA distributions developed in the 0.2 Zr and 1.0 Zr tensile samples, respectively. In the case of 0.2 Zr sample, the $\langle uvt0\rangle$-type IGMA distributions are developed in G1, G4, and G6 grains, suggesting the activation of basal $\langle a\rangle$ slips. Thus, it could be inferred that the basal slip and extension twinning dominated the deformation of the 0.2 Zr sample. While in the case of the 1.0 Zr sample, a higher level of stored energy, as indicated in KAM diagrams, triggered multiple slips in the homogeneous fine-grained microstructure. As depicted in Fig. 16(d), the preferential IGMA around the $\langle 0001\rangle$ axis (G7), $\langle 01\bar{1}0\rangle$ axis (G10 and G11), and $\langle uvt0\rangle$ axes (G8, G9 and G12) are observed, corresponding to the characteristics of the prismatic $\langle a\rangle$, and basal $\langle a\rangle$ or pyramidal II $\langle c+a\rangle$ slips, respectively. Considering a very high CRSS value of pyramidal II $\langle c+a\rangle$ slip at ambient temperature, basal, prismatic $\langle a\rangle$ slips and extension twinning should dominate the tensile deformation of the 1.0 Zr sample.

Consequently, Zr addition plays a significant role in the mechanical properties of Mg−1.0Yb as-cast alloy. Firstly, a sufficient amount of Zr addition promoted the grain refinement and particle precipitation, considerably improving the tensile strength by grain boundary (HAGBs and TBs) particle dispersion, and solution strengthening. Secondly, the sufficient Zr addition combined with Yb solute may lead to the operation of multiple slip systems and promote the activity of extension twinning during stretching, thus greatly enhancing the ductility.

4.3 Temporal evolution of bulk corrosion in 1.0 Zr sample

From the above analysis, it could be concluded that the corrosion resistance of as-cast Mg−1.0Yb alloy was significantly improved via a slightly excessive 1.0 wt.% Zr addition. Nevertheless, the question was still open as to how the corrosion behavior evolved with extended immersion durations. Elucidating the temporal evolution of corrosion behavior was beneficial to a deeper and more comprehensive understanding of the corrosion mechanism underlying this well-performed Mg−1.0Yb−1.0Zr alloy.

Figure 17 shows the EIS analysis results of the Mg−1.0Yb−1.0Zr alloys immersed in SBF solution at 37 °C for different time. The electrochemical polarization parameters including the φ_{corr}, J_{corr}, and η_{corr} are listed in Table 7. With increasing immersion durations from 15 min to 120 h, the φ_{corr} became nobler in comparison with a substantial decrease in the J_{corr} (Fig. 17(a)) as well as a considerable increase in the impedances (Figs. 17(b) and (c)). Consistently, the peaks as demonstrated in Fig. 17(d) move to the low-frequency regions, indicating that the electrochemical reaction gradually weakens with extended immersion time [40]. In addition, the phase angle of the peaks gradually increases, further suggesting that a more integrated and protective corrosion layer is developed during long-term immersion [41,42]. The speculation deduced from the EIS spectra is in a good agreement with the characteristics of the corrosion rate curve as demonstrated in Fig. 6. All these features indicated that a decrease in degradation rate with advancing corrosion was achieved in the Mg−1.0Yb−1.0Zr alloy.

Specifically, the micro-galvanic couple between the fine Zr-rich particles and the matrix rapidly eroded the alloy surface in the initial corrosion, resulting in a severe local corrosion attack, which corresponded to the inductive characteristic in the Nyquist low-frequency region for the sample with a short immersion time. With advancing corrosion, the low-frequency inductive

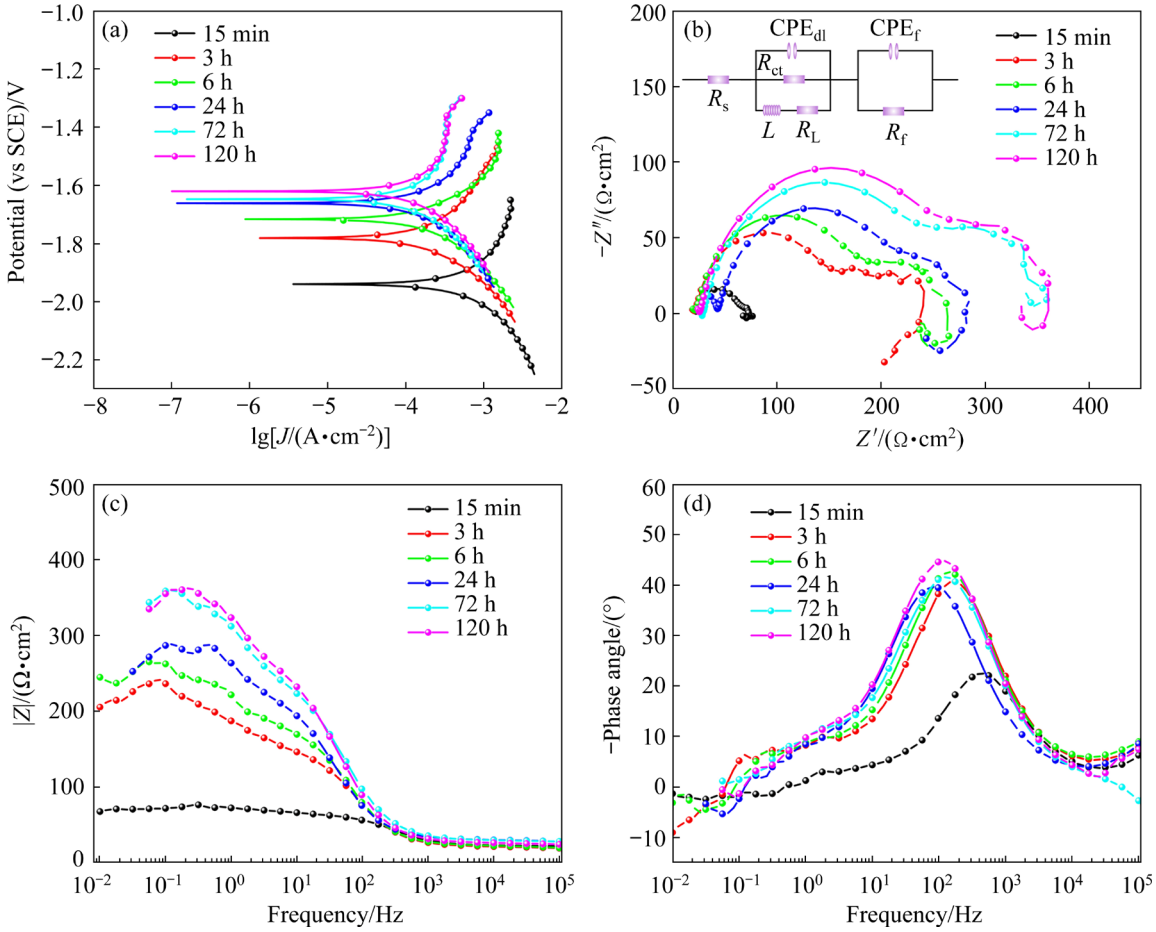

Fig. 17 Potentiodynamic polarization curves (a), Nyquist plots (b), Bode impedance plots (c), and Bode phase angle plots (d) of Mg−1.0Yb−1.0Zr alloy immersed in SBF solution at 37 °C for different time

loop weakened to some extent, indicating that the local corrosion of the substrate was suppressed and the protection of the film was substantially improved. This feature is visible in the surface (Fig. 7) and cross-sectional (Fig. 9) corrosion morphologies of the alloy after a long-term immersion. The enhancement in corrosion resistance and degradation uniformity of the 1.0 Zr sample should be related to the fact that the dispersed and finely distributed Zr-rich particles are in favor of the formation of a continuous, compact, and thick corrosion product film after a long-term immersion. This phenomenon was also observed in the Mg−2Zn−0.3Ca corrosion [43]. Furthermore, to quantitatively evaluate the temporal evolution of film protection during corrosion, the equivalent circuit model shown in Fig. 17(b) was employed to determine the electrochemical impedance parameters, as listed in Table 8.

In the aforementioned research examining the corrosion performance of the 1.0 Zr sample over varying immersion durations, it was observed that the corrosion rate of the alloy decreased consistently as the immersion time increased. This finding suggested that the corrosion resistance of the alloy continued to improve. The implication here was that the protective corrosion film in the alloy thickened as the immersion time prolonged. Available investigations substantiated that the thickness of the protective film may serve as an indicator of the corrosion layer's protection, which can be estimated by the variation of the effective capacitance (C_{eff}) corresponding to the film by the Brug formula [44,45]:

$$C_{\text{eff}} = Q_{\text{dl}}^{1/n}\left(\frac{1}{R_{\text{s}}}+\frac{1}{R_{\text{ct}}}\right)^{\frac{n-1}{n}} \tag{4}$$

where Q_{dl} is the admittance of the CPE_{dl}, and n is the CPE_{dl} parameter. Notably, the effective capacitance gradually decreased from 25.66 to 17.59 μF/cm^2, while the charge transfer resistance increased from 27.57 to 208.33 Ω·cm^2 as the immersion time prolonged. These trends indicated that the cathodic reaction became more challenging [46], signifying an enhancement in the protection of the corrosion layer throughout the extended immersion period [47]. This finding aligned with the declining corrosion rate observed in the mass loss analysis (Fig. 6). It was worth mentioning that

Table 7 Electrochemical parameter fitting results in polarization curves of Mg−1.0Yb−1.0Zr alloy immersed in SBF solution at 37 °C for different time

Immersion time/h	φ_{corr}(vs SCE)/ V	β_{a}/ (mV·decade^{-1})	$-\beta_{\text{c}}$/ (mV·decade^{-1})	R_{p}/ (Ω·cm^2)	J_{corr}/ (μA·cm^{-2})	η_{corr}/ (mm·a^{-1})
0.25	−1.939	271	183	106	449	10.26
3	−1.781	317	201	273	196	4.48
6	−1.716	172	216	251	166	3.79
24	−1.661	290	204	362	144	3.29
72	−1.647	458	204	476	129	2.95
120	−1.620	362	201	480	117	2.67

Table 8 Fitting values of EIS impedance spectrum equivalent circuit of Mg−1.0Yb−1.0Zr alloy immersed in SBF solution at 37 °C for different time

Immersion time/h	R_{s}/ (Ω·cm^2)	R_{f}/ (Ω·cm^2)	CPE_{f}/ (Ω^{-1}·cm^2·s^n)	n_1	R_{ct}/ (Ω·cm^2)	CPE_{dl}/ (Ω^{-1}·cm^2·s^n)	n_2	R_{L}/ (Ω·cm^2)	L/ (H·cm^2)
0.25	21.12	27.83	3.82×10^{-3}	0.43	27.57	3.27×10^{-5}	0.96	77.66	312
3	19.43	182.70	4.08×10^{-3}	0.43	97.38	3.78×10^{-5}	0.94	32.51	911
6	20.91	194.42	3.45×10^{-3}	0.46	120.92	3.75×10^{-5}	0.93	46.66	807
24	28.83	307.13	4.56×10^{-3}	0.46	161.52	5.08×10^{-5}	0.88	68.52	423
72	28.49	456.92	2.61×10^{-3}	0.52	176.72	4.56×10^{-5}	0.88	82.78	265
120	25.26	466.61	3.17×10^{-3}	0.53	208.33	5.27×10^{-5}	0.86	73.36	362

although this study did not directly observe the nanoscale protective layer, the calculations conducted confirmed the thickening of the protective layer during long-term erosion. This offered another plausible explanation for the improved corrosion resistance observed in the Mg−1.0Yb−1.0Zr alloy, wherein a slightly excessive amount of Zr was added.

5 Conclusions

(1) The addition of Zr contributes to the refinement and equalization of the as-cast microstructure, which is in favor of the mechanical properties of the Mg−1.0Yb master alloy. With increasing Zr addition, the homogenization of the grain structure and the coarsening of Zr-rich particles tend to be evident, and a homogeneous microstructure with dispersedly distributed fine Zr-rich particles developed in the Mg−1.0Yb−1.0Zr alloy.

(2) The corrosion of the Mg−Yb−Zr alloy is Zr-content dependent. A trace or excessive Zr addition results in severe micro-galvanic corrosion due to the heterogeneous grain structure with an initial potential difference and the accelerated cathode reaction induced by the coarsening of the Zr-rich particles, respectively. The Zr-free and 1.0 Zr alloyed counterparts generally exhibit uniform corrosion and a similar degradation history during long-term immersion in SBF solution.

(3) The excellent corrosion resistance of the Mg−1.0Yb−1.0Zr alloy is rooted in a slightly excessive Zr addition relative to the solubility of Zr in Mg, which greatly homogenizes the grain structure and disperses the fine Zr-rich particles, thus alleviating the initial potential difference, developing a continuous corrosion products film, thickening the protective layer, and improving the stability and adhesion of the corrosion film.

(4) The in vitro biocompatibility testing demonstrates that the Zr-containing Mg−1.0Yb alloys possess desirable cytocompatibility and hemocompatibility. Impressively, the Mg−1.0Yb−1.0Zr alloy exhibits a favorable combination with a tensile yield strength of ~53 MPa, elongation of ~9.8%, and corrosion rate of ~2.08 mm/a, suggesting a promising candidate for biomedical applications due to the good synergy between the mechanical properties and the biocorrosion resistance.

CRediT authorship contribution statement

Zhuo-zhang WEN: Writing − Original draft, Formal analysis, Visualization, Data curation; **Lu LI:** Conceptualization, Writing − Review & editing, Funding acquisition; **Xue BAI:** Formal analysis, Validation; **Wei ZHOU:** Formal analysis, Investigation; **Zhen-ni ZHOU:** Validation; **Peng XUE**, **Jing LI** and **Xian-quan JIANG:** Formal analysis.

Declaration of competing interest

The authors declare that they have no known competing financial interests or personal relationships that could have appeared to influence the work reported in this paper.

Acknowledgments

The authors are grateful for the financial supports from the China Scholarship Council (No. 201808505057).

References

[1] SHIRI M, JAFARI H, SINGH R. Effect of extrusion parameters on degradation of magnesium alloys for bioimplant applications: A review [J]. Transactions of Nonferrous Metals Society of China, 2022, 32: 2787−2813.

[2] GRGUR B N, JUGOVIĆ B Z, GVOZDENOVIĆ M M. Influence of chloride ion concentration on initial corrosion of AZ63 magnesium alloy [J]. Transactions of Nonferrous Metals Society of China, 2022, 32: 1133−1143.

[3] WANG G Q, WANG S R, YANG X F, WEN D S, GUO Y. Microstructure, mechanical properties and fretting corrosion wear behavior of biomedical ZK60 Mg alloy treated by laser shock peening [J]. Transactions of Nonferrous Metals Society of China, 2023, 33: 1715−1728.

[4] SUN M, WU G H, WANG W, DING W J. Effect of Zr on the microstructure, mechanical properties and corrosion resistance of Mg−10Gd−3Y magnesium alloy [J]. Materials Science and Engineering: A, 2009, 523: 145−151.

[5] JAFARI H, AMIRYAVARI P. The effects of zirconium and beryllium on microstructure evolution, mechanical properties and corrosion behaviour of as-cast AZ63 alloy [J]. Materials Science and Engineering: A, 2016, 654: 161−168.

[6] KIANI F, LIN J X, VAHID A, MUNIR K, WEN C E, LI Y C. Mechanical and corrosion properties of extruded Mg−Zr−Sr alloys for biodegradable implant applications [J]. Materials Science and Engineering: A, 2022, 831: 142192.

[7] QIAN M, STJOHN D H, FROST M T. Characteristic zirconium-rich coring structures in Mg−Zr alloys [J]. Scripta Materialia, 2002, 46: 649−654.

[8] HUAN Z G, LEEFLANG M A, ZHOU J, FRATILA-APACHITEI L E, DUSZCZYK J. In vitro degradation behavior and cytocompatibility of Mg−Zn−Zr alloys [J]. Journal of Materials Science: Materials in Medicine, 2010, 21: 2623−2635.

[9] JIA Q G, ZHANG W X, SUN Y, XU C X, ZHANG J S, KUAN J. Microstructure and mechanical properties of as-cast and extruded biomedical Mg−Zn−Y−Zr−Ca alloy at different temperatures [J]. Transactions of Nonferrous Metals Society of China, 2019, 29: 515−525.

[10] CAO F Y, ZHANG J, LI K K, SONG G L. Influence of heat treatment on corrosion behavior of hot rolled Mg_5Gd alloys [J]. Transactions of Nonferrous Metals Society of China, 2021, 31: 939−951.

[11] LIAO G L, WU G H, LIU W C, SUN J W, XIAO L, PANG S, CHEN P J. Microstructure evolution and enhanced fatigue behavior in the Mg−10Li−5Zn−0.5Er alloys micro-alloyed with Yb [J]. Journal of Magnesium and Alloys, 2024, 12: 3159−3175.

[12] LI L, WANG Y, LI H, JIANG W, WANG T, ZHANG C C, WANG F, GARMESTANI H. Effect of the Zener−Hollomon parameter on the dynamic recrystallization kinetics of Mg−Zn−Zr−Yb magnesium alloy [J]. Computational Materials Science, 2019, 166: 221−229.

[13] LV H, LI L, WEN Z Z, LIU C R, ZHOU W, BAI X, ZHONG H. Effects of extrusion ratio and temperature on the microstructure and mechanical properties of Mg−Zn−Yb−Zr extrusion alloys [J]. Materials Science and Engineering: A, 2022, 833: 142521.

[14] LI L, WANG T, WANG Y, ZHANG C C, LV H, LIN H, YU W B, HUANG C J. Effects of ytterbium addition and heat treatment on the mechanical properties and biocorrosion behaviors of Mg−Zn−Zr alloy [J]. Journal of Magnesium and Alloys, 2020, 8: 499−509.

[15] LI L, WANG T, HOU M M, XUE P, LV H, HUANG C J. In vitro degradation behavior and biocompatibility of Mg−5.8Zn−2.0Yb−0.5 Zr alloy during aging treatment [J]. Materials Letters, 2021, 282: 128682.

[16] LI L, ZHANG C C, LV H, LIU C R, WEN Z Z, JIANG J W. Texture development and tensile properties of Mg−Yb binary alloys during hot extrusion and subsequent annealing [J]. Journal of Magnesium and Alloys, 2022, 10: 249−265.

[17] KOKUBO T, TAKADAMA H. How useful is SBF in predicting in vivo bone bioactivity? [J]. Biomaterials, 2006, 27: 2907−2915.

[18] STERN M, GEARY A L. Electrochemical polarization: I. A theoretical analysis of the shape of polarization curves [J]. Journal of the Electrochemical Society, 1957, 104: 751.

[19] SHI Z M, LIU M, ATRENS A. Measurement of the corrosion rate of magnesium alloys using Tafel extrapolation [J]. Corrosion Science, 2010, 52: 579−588.

[20] MOHAMMADI-ZERANKESHI M, ALIZADEH R, LABBAF S. Improving mechanical, degradation and biological behavior of biodegradable Mg−2Ag alloy: Effects of Y addition and heat treatment [J]. Journal of Materials Research and Technology, 2023, 22: 1677−1694.

[21] DHANAPAL A, RAJENDRA BOOPATHY S, BALASUBRAMANIAN V. Influence of pH value, chloride ion concentration and immersion time on corrosion rate of friction stir welded AZ61A magnesium alloy weldments [J]. Journal of Alloys and Compounds, 2012, 523: 49−60.

[22] NIU H Y, DENG K K, NIE K B, CAO F F, ZHANG X C, LI W G. Microstructure, mechanical properties and corrosion properties of Mg−4Zn−xNi alloys for degradable fracturing ball applications [J]. Journal of Alloys and Compounds, 2019, 787: 1290−1300.

[23] LIU J H, SONG Y W, CHEN J C, CHEN P, SHAN D Y, HAN E Y. The special role of anodic second phases in the micro-galvanic corrosion of EW75 Mg alloy [J]. Electrochimica Acta, 2016, 189: 190−195.

[24] NORDLIEN J H, ONO S, MASUKO N, NIS¸ANCIOĞLU K. Morphology and structure of oxide films formed on magnesium by exposure to air and water [J]. Journal of the Electrochemical Society, 1995, 142: 3320−3322.

[25] MÜLLER L, MÜLLER F A. Preparation of SBF with different HCO_3-content and its influence on the composition of biomimetic apatites [J]. Acta Biomaterialia, 2006, 2: 181−189.

[26] KALB H, RZANY A, HENSEL B. Impact of microgalvanic corrosion on the degradation morphology of WE43 and pure magnesium under exposure to simulated body fluid [J]. Corrosion Science, 2012, 57: 122−130.

[27] SONG Y W, SHAN D Y, CHEN R S, ZHANG F, HAN E H. Biodegradable behaviors of AZ31 magnesium alloy in simulated body fluid [J]. Materials Science and Engineering: C, 2009, 29: 1039−1045.

[28] ZHANG N, SUN N, DENG C. A hydrophilic magnetic MOF for the consecutive enrichment of exosomes and exosomal phosphopeptides [J]. Chemical Communications, 2020, 56: 13999−14002.

[29] ZHAO Y M, SHAN X C, AN Q D, XIAO Z Y, ZHAI S R. Interfacial integration of zirconium components with amino-modified lignin for selective and efficient phosphate capture [J]. Chemical Engineering Journal, 2020, 398: 125561.

[30] WANG Y K, GOU Z R, MA S Y, JIN Z H, CHEN S, YE J, NIE Z G, WAN Z H, ZHANG C D, YE Y X, YU X H, YE Z M, REN Y J. Remote eradication of delayed infection on orthopedic implants via magnesium-based total morphosynthesis of biomimetic mineralization strategy [J]. Materials & Design, 2023, 233: 112233.

[31] WU J X, CAO X, XU C X, DONG Y H, DI X M, ZHANG J S. Effect of Sr on the microstructure and corrosion properties of the as-cast Mg−Zn−Zr alloy [J]. International Journal of Materials Research, 2022, 113: 194−204.

[32] ZENG R C, KAINER K U, BLAWERT C, DIETZEL W. Corrosion of an extruded magnesium alloy ZK60 component: The role of microstructural features [J]. Journal of Alloys and Compounds, 2011, 509: 4462−4469.

[33] BI G L, LI Y D, ZANG S J, ZHANG J B, MA Y, HAO Y. Microstructure, mechanical and corrosion properties of Mg−2Dy−xZn (x=0, 0.1, 0.5 and 1 at.%) alloys [J]. Journal of Magnesium and Alloys, 2014, 2: 64−71.

[34] LI C Q, XU D K, ZENG Z R, WANG B J, SHENG L Y, CHEN X B, HAN E H. Effect of volume fraction of LPSO phases on corrosion and mechanical properties of Mg−Zn−Y alloys [J]. Materials & Design, 2017, 121: 430−441.

[35] SRINIVASAN A, HUANG Y, MENDIS C L, BLAWERT C, KAINER K U, HORT N. Investigations on microstructures, mechanical and corrosion properties of Mg−Gd−Zn alloys [J]. Materials Science and Engineering A, 2014, 595: 224−234.

[36] YANG M B, LIANG X F, YI Z, PAN F S. Effects of zirconium addition on as-cast microstructure and mechanical properties of Mg−3Sn−2Ca magnesium alloy [J]. Materials & Design, 2011, 32: 1967−1973.
[37] ZHANG B, HOU Y L, WANG X D, WANG Y, GENG L. Mechanical properties, degradation performance and cytotoxicity of Mg−Zn−Ca biomedical alloys with different compositions [J]. Materials Science and Engineering: C, 2011, 31: 1667−1673.
[38] CHAUDRY U M, KIM T H, KIM Y S, HAMAD K, KO Y G, KIM J G. Dynamic recrystallization behavior of AZ31-0.5Ca magnesium alloy during warm rolling [J]. Materials Science and Engineering: A, 2019, 762: 138085.
[39] CHUN Y B, DAVIES C H J. Investigation of prism 〈*a*〉 slip in warm-rolled AZ31 alloy [J]. Metallurgical and Materials Transactions A, 2011, 42: 4113−4125.
[40] RAJENDRAN R, DONDAPATI S. Insights of microstructural features and their effect on degradation and the in vitro bioactivity response of as-cast Mg−Sn alloys for orthopedic implant applications [J]. Materials, 2022, 15: 6327.
[41] MAJHI J, GANGULY S, BASU A, MONDAL A K. Improved corrosion response of squeeze-cast AZ91 magnesium alloy with calcium and bismuth additions [J]. Journal of Alloys and Compounds, 2021, 873: 159600.
[42] FENG H, LIU S H, DU Y, LEI T, ZENG R C, YUAN T C. Effect of the second phases on corrosion behavior of the Mg−Al−Zn alloys [J]. Journal of Alloys and Compounds, 2017, 695: 2330−2338.
[43] YANG L Z, FENG Y, HE Y Q, YANG L Y, LIU H C, WANG X, PENG C Q, WANG R C. Effect of Sc/Sm microalloying on microstructural and properties of Mg−2Zn−0.3Ca biodegradable alloy [J]. Journal of Alloys and Compounds, 2022, 907: 164533.
[44] BRUG G J, VAN DEN EEDEN A L G, SLUYTERS-REHBACH M, SLUYTERS J H. The analysis of electrode impedances complicated by the presence of a constant phase element [J]. Journal of Electroanalytical Chemistry and Interfacial Electrochemistry, 1984, 176: 275−295.
[45] HIRSCHORN B, ORAZEM M E, TRIBOLLET B, VIVIER V, FRATEUR I, MUSIANI M. Determination of effective capacitance and film thickness from constant-phase-element parameters [J]. Electrochimica Acta, 2010, 55: 6218−6227.
[46] LIU Y X, CURIONI M, LIU Z. Correlation between electrochemical impedance measurements and corrosion rates of Mg−1Ca alloy in simulated body fluid [J]. Electrochimica Acta, 2018, 264: 101−108.
[47] ASCENCIO M, PEKGULERYUZ M, OMANOVIC S. An investigation of the corrosion mechanisms of WE43 Mg alloy in a modified simulated body fluid solution: The influence of immersion time [J]. Corrosion Science, 2014, 87: 489−503.

Zr 添加对铸态 Mg−1.0Yb 合金力学性能和体外降解行为的影响

文镯璋，李 路，白 雪，周 伟，周珍妮，薛 鹏，李 婧，蒋显全

西南大学 材料与能源学院，重庆 400715

摘 要：研究 Zr 添加对铸态 Mg−1.0Yb−*x*Zr (*x*=0，0.2，1.0 和 1.5，质量分数，%)合金力学性能和体外降解行为的影响。结果表明，随 Zr 含量的增加，Mg−1.0Yb 铸态合金晶粒逐渐由典型的柱状晶转变为等轴细晶粒，同时伴随着富 Zr 颗粒的出现和粗化。电化学和浸泡试验结果表明，Zr 添加量对合金的腐蚀具有重要影响。微量或过量 Zr 添加会导致严重的局部腐蚀，而无添加和添加 1.0 Zr 的合金趋向于均匀腐蚀。在 Mg−1.0Yb−1.0Zr 合金中观察到的良好力学和耐腐蚀性能，得益于其均匀的等轴细晶结构和细小弥散分布的富 Zr 颗粒。晶粒细化显著提升了合金的综合力学性能，在长期浸泡过程中产生更稳定、致密的钝化膜降低了腐蚀速率，有效提升合金的耐腐蚀性能。

关键词：镁镱合金；锆添加；显微组织；力学性能；腐蚀行为

(Edited by Wei-ping CHEN)